



**COMPARISON OF IMAGE PROCESSING
TECHNIQUES USING RANDOM NOISE RADAR**

THESIS

Jesse Robert B. Cruz, Capt, USAF

AFIT-ENG-14-M-22

**DEPARTMENT OF THE AIR FORCE
AIR UNIVERSITY**

AIR FORCE INSTITUTE OF TECHNOLOGY

Wright-Patterson Air Force Base, Ohio

Distribution Statement A:
Approved for Public Release; Distribution Unlimited

The views expressed in this thesis are those of the author and do not reflect the official policy or position of the United States Air Force, the Department of Defense, or the United States Government.

This material is declared a work of the U.S. Government and is not subject to copyright protection in the United States.

COMPARISON OF IMAGE PROCESSING
TECHNIQUES USING RANDOM NOISE RADAR

THESIS

Presented to the Faculty
Department of Electrical and Computer Engineering
Graduate School of Engineering and Management
Air Force Institute of Technology
Air University
Air Education and Training Command
in Partial Fulfillment of the Requirements for the
Degree of Master of Science in Electrical Engineering

Jesse Robert B. Cruz, B.S.E.E.

Capt, USAF

March 2014

Distribution Statement A:
Approved for Public Release; Distribution Unlimited

COMPARISON OF IMAGE PROCESSING
TECHNIQUES USING RANDOM NOISE RADAR

Jesse Robert B. Cruz, B.S.E.E.
Capt, USAF

Approved:

//signed//

Peter J. Collins, PhD (Chairman)

17 Mar 2014

Date

//signed//

Julie A. Jackson, PhD (Member)

17 Mar 2014

Date

//signed//

Richard K. Martin, PhD (Member)

17 Mar 2014

Date

Abstract

Radar imaging is a tool used by our military to provide information to enhance situational awareness for both warfighters on the front lines and military leaders planning and forming strategies from afar. Noise radar technology is especially exciting as it has properties of covertness as well as the ability to see through walls, foliage, and other types of cover.

In this thesis, Air Force Institute of Technology (AFIT)'s noise radar network (NoNet) was used to generate images utilizing a random noise radar waveform as the transmission signal. The NoNet was arranged in four configurations: arc, line, cluster, and surround. Images were formed using three algorithms: multilateration and the synthetic aperture radar (SAR) imaging techniques, convolution backprojection, and polar format algorithm. Each configuration was assessed based on image quality, in terms of its resolution, and computational complexity, in terms of its execution time.

Experiments revealed tradeoffs between computational complexity and achieving fine resolutions. Depending on image size, the multilateration algorithm was approximately 6 to 35 faster than polar format and 16 to 26 times faster than convolution backprojection. Backprojection yielded images with resolutions up to approximately 11 times finer in range and 18 times finer in cross-range for the surround configuration, over multilateration images. Pixel size in polar format images made comparisons of resolution unusable.

This thesis provides information on the performance of imaging algorithms given a configuration of nodes. The information will provide groundwork for future use of the AFIT NoNet as a covertly operating imaging radar in dynamic applications.

Acknowledgments

I would like to thank my family, all of my friends, and the AFIT faculty for your support throughout this work.

Jesse Robert B. Cruz

Table of Contents

	Page
Abstract	iv
Acknowledgments	v
Table of Contents	vi
List of Figures	viii
List of Tables	xii
List of Acronyms	xiv
I. Introduction	1
1.1 Problem Statement	1
1.2 Motivation	2
1.3 Research Goals	3
1.4 Thesis Layout	4
II. Theory and Background	6
2.1 Noise Radar	6
2.1.1 Noise Radar Characteristics	6
2.1.2 Noise Radar Transmission	9
2.1.3 Noise Radar Correlation Receiver	11
2.1.4 AFIT NoNet (Noise Network)	12
2.2 Radar Imaging	16
2.2.1 Multilateration Imaging	19
2.2.2 Synthetic Aperture Radar (SAR) Imaging	21
2.2.2.1 Polar Format Imaging	24
2.2.2.2 Convolution Backprojection Imaging	26
2.3 Chapter Conclusion	28
III. Methodology	29
3.1 Data Collection Parameters and Method	29
3.2 Node Configurations	33
3.2.1 Arc Configuration	34

	Page
3.2.2 Line Configuration	36
3.2.3 Cluster Configuration	38
3.2.4 Surround Configuration	40
3.3 Image Formation, Resolution Measuring, Computation Timing	42
3.3.1 Multilateration Algorithm	42
3.3.2 Backprojection Algorithm	44
3.3.3 Polar Format Algorithm	45
3.3.4 Determination of Resolution	46
3.3.5 Timing For Computational Complexity	47
3.4 Chapter Summary	47
 IV. Results	 49
4.1 Image Results of the Arc Configuration	49
4.1.1 Arc Image Results Using Multilateration	49
4.1.2 Arc Image Results Using Convolution Backprojection	53
4.1.3 Arc Image Results Using Polar Format Algorithm	56
4.2 Image Results of the Line Configuration	57
4.2.1 Line Image Results Using Multilateration	58
4.2.2 Line Image Results Using Convolution Backprojection	60
4.2.3 Line Image Results Using Polar Format Algorithm	63
4.3 Image Results of the Cluster Configuration	65
4.3.1 Cluster Image Results Using Multilateration	65
4.3.2 Cluster Image Results Using Convolution Backprojection	68
4.3.3 Cluster Image Results Using Polar Format Algorithm	71
4.4 Image Results of the Surround Configuration	72
4.4.1 Surround Image Results Using Multilateration	72
4.4.2 Surround Image Results Using Convolution Backprojection	74
4.4.3 Surround Image Results Using Polar Format Algorithm	77
4.5 Comparison of Results	78
 V. Conclusions	 86
5.1 Review of Research Goals	86
5.2 Research Results and Contributions	86
5.3 Future Work	87
 Bibliography	 90

List of Figures

Figure	Page
2.1 The ambiguity function of a pseudo-random noise signal created in Matlab. Noise signals have a thumbtack ambiguity function and are capable of achieving high range and Doppler resolution.	9
2.2 A NoNet radar node. Each node consists of a computer, noise radar box, transmit and receive antennas, and a battery power source (note an AC power source may also be used).	13
2.3 Block diagram of AFIT NoNet.	14
2.4 A sample of the raw transmitted noise waveform.	15
2.5 Histogram of the transmission signal shown in Figure 2.4. The histogram shows that the signal has a Gaussian distribution.	15
2.6 The raw received waveform from the transmitted signal shown in Figure 2.4.	17
2.7 Histogram of the received signal shown in Figure 2.6. The histogram shows that the received signal kept Gaussian distribution.	17
2.8 The frequency spectrum of the transmitted signal shown in Figure 2.4.	18
2.9 Example of a 1×4 (one transmitter/four receiver) multistatic location estimate using multilateration of isorange contours for target position (reproduced from [14]).	21
2.10 A representation of phase history of a spotlight SAR system	25
2.11 Illustration of interpolation from polar to Cartesian raster	25
3.1 Lab space where all radar data was collected.	30
3.2 Diagram of the room for visual aid	31

Figure	Page
3.3 Plot illustrating the relationships between the radar's run time, acquisitions, triggers, and sampling period. The sampling frequency is 6000 Msamp/s, each acquisition consists of 15 triggers per acquisition.	34
3.4 Arc Configuration - The relative positions of the walls and significant clutter are indicated in the figure, see also Figure 3.2.	35
3.5 Line Configuration - The relative positions of the walls and significant clutter are indicated in the figure, see also Figure 3.2.	37
3.6 Cluster Configuration - The relative positions of the walls and significant clutter are indicated in the figure, see also Figure 3.2.	39
3.7 Surround Configuration - The relative positions of the walls and significant clutter are indicated in the figure, see also Figure 3.2.	41
4.1 Arc configuration multilateration image. The node locations are indicated by white squares and the actual target location is indicated by a white circle.	50
4.2 Arc configuration multilateration image in dB with -3 dB threshold. The node locations are indicated by white squares and the actual target location is indicated by a white circle.	50
4.3 Range profiles collected by the nodes in the arc configuration. See also Figure 3.4.	51
4.4 Arc configuration backprojection image. The node and target locations are indicated by white squares and a white circle, respectively.	54
4.5 Arc configuration convolution backprojection image in dB with -3 dB threshold. The node and target locations are indicated by white squares and a white circle, respectively.	54
4.6 Arc configuration polar format image.	57
4.7 Arc configuration polar format image in dB with -3 dB threshold.	57

Figure	Page
4.8 Line configuration multilateration image. The node and target locations are indicated by white squares and a white circle, respectively.	59
4.9 Line configuration multilateration image in dB with -3 dB threshold. The node and target locations are indicated by white squares and a white circle, respectively.	59
4.10 Line configuration image rotated so that range and cross-range are in the y and x directions, respectively.	60
4.11 Line configuration backprojection image. The node and target locations are indicated by white squares and a white circle, respectively.	61
4.12 Line configuration backprojection image in dB with -3 dB threshold. The node and target locations are indicated by white squares and a white circle, respectively.	61
4.13 Line configuration image rotated so that range and cross-range are in the y and x directions, respectively.	62
4.14 Line configuration polar format image.	64
4.15 Line configuration polar format image in dB with -3 dB threshold.	64
4.16 Cluster configuration multilateration image. The node and target locations are indicated by white squares and a white circle, respectively.	66
4.17 Cluster configuration multilateration image in dB with -3 dB threshold. The node and target locations are indicated by white squares and a white circle, respectively.	66
4.18 Cluster configuration image rotated so that range and cross-range are in the y and x directions, respectively.	67
4.19 Cluster configuration backprojection image. The node and target locations are indicated by white squares and a white circle, respectively.	69

Figure	Page
4.20 Cluster configuration backprojection image in dB with -3 dB threshold. The node and target locations are indicated by white squares and a white circle, respectively.	69
4.21 Cluster configuration image rotated so that range and cross-range are in the y and x directions, respectively.	70
4.22 Cluster configuration polar format image.	72
4.23 Cluster configuration polar format image in dB with -3 dB threshold.	72
4.24 Surround configuration multilateration image. The node and target locations are indicated by white squares and a white circle, respectively.	74
4.25 Surround configuration multilateration image in dB with -3 dB threshold. The node and target locations are indicated by white squares and a white circle, respectively.	74
4.26 Surround configuration backprojection image. The node and target locations are indicated by black squares and a black circle, respectively.	76
4.27 Surround configuration backprojection image in dB with -3 dB threshold. The node and target locations are indicated by white squares and a white circle, respectively.	76
4.28 Surround configuration image plot in 3D. The target can be made out with very fine resolution due to the nearly 360° azimuth, however poor azimuth sampling results in a poor alias free image diameter.	77
4.29 Surround configuration polar format image. The node and target locations are indicated by white squares and a white circle, respectively.	79
4.30 Surround configuration polar format image in dB with -3 dB threshold. The node and target locations are indicated by white squares and a white circle, respectively.	79

List of Tables

Table	Page
3.1 Noise Network Parameters	33
3.2 Arc Configuration	36
3.3 Line Configuration	38
3.4 Cluster Configuration	40
3.5 SurroundConfiguration	42
3.6 Expected Range and Cross-range Resolutions and Un-alaised Range and Cross Range Extents for SAR Images	47
4.1 Computational complexity for the Arc configuration using Multilateration (Execution time is the average of 20 imaging instances).	53
4.2 Resolution results for the backprojection algorithm performed on the arc configuration.	55
4.3 Computational complexity for the Arc configuration using Backprojection (Execution time is the average of 20 imaging instances).	56
4.4 Computational complexity for the Arc configuration using Polar Format Algorithm.	58
4.5 Computational complexity for the Line configuration using Multilateration (Execution time is the average of 20 imaging instances)	60
4.6 Resolution results for the backprojection algorithm performed on the line configuration.	62
4.7 Computational complexity for the Line configuration using Convolution Backprojection (Execution time is the average of 20 imaging instances).	63
4.8 Computational complexity for the Line configuration using Polar Format Algorithm.	65

Table	Page
4.9 Computational complexity for the Cluster configuration using Multilateration (Execution time is the average of 20 imaging instances).	68
4.10 Resolution results for the backprojection algorithm performed on the cluster configuration.	70
4.11 Computational complexity for the Cluster configuration using Convolution Backprojection (Execution time is the average of 20 imaging instances).	71
4.12 Computational complexity for the Cluster configuration using Polar Format Algorithm.	73
4.13 Computational complexity for the Surround configuration using Multilatera- tion (Execution time is the average of 20 imaging instances).	75
4.14 Resolution results for the backprojection algorithm performed on the surround configuration.	75
4.15 Computational complexity for the Surround configuration using Convolution Backprojection (Execution time is the average of 20 imaging instances).	78
4.16 Computational complexity for the Surround configuration using Polar Format Algorithm.	80
4.17 Summary table of all execution times	81
4.18 Multilateration verses polar format execution times.	82
4.19 Multilateration verses convolution backprojection execution times.	82
4.20 Polar format verses convolution backprojection execution times.	83
4.21 Execution time for the polar format algorithm broken out by interpolation time and image formation time.	84
4.22 Summary table of all measured resolutions	85

List of Acronyms

Acronym	Definition
AFIT	Air Force Institute of Technology
SAR	synthetic aperture radar
EM	electromagnetic
LFM	linear frequency modulated
NoNet	noise radar network
UAV	unmanned aerial vehicle
LPI	low probability of interception
LPD	low probability of detection
UWB	ultra-wideband
EM	electromagnetic
CW	continuous wave
RCS	radar cross section
RFI	radio frequency interference
FFT	fast Fourier transform
IFFT	inverse fast Fourier transform
WGN	white Gaussian noise
IID	independent and identically distributed
ECM	Electronic counter measure
ECCM	electronic counter countermeasure
GPS	global positioning system
LOS	line of sight
SNR	signal to noise ratio
A/D	analog to digital

COMPARISON OF IMAGE PROCESSING TECHNIQUES USING RANDOM NOISE RADAR

I. Introduction

1.1 Problem Statement

Radio Detection and Ranging, or Radar, has long been a part of military history. In the 1930s several countries, including the United States, simultaneously and independently began research and development in the use of radio echoes to detect enemy ships and aircraft [21]. Since then, radar technology has evolved from use for simple detection and ranging to much more complicated applications, such as high resolution imaging using synthetic aperture radar (SAR).

Conventional radar systems use deterministic electromagnetic (EM) waveforms, such as sinusoidal or linear frequency modulated (LFM) waves, that an adversary can easily intercept and identify. Knowledge of a radar's waveform make a radar system susceptible to attack in the form of deception (creating false targets) or jamming (concealing actual targets).

Noise radar differs from conventional radar in its use of random noise waveforms to interrogate a scene of interest. The truly random nature of a noise radar's waveform give their systems inherent properties with defense against detection, deception, and jamming [24]. Additionally, noise radar waveforms are classified as ultra-wideband (UWB) making the technology attractive for use because the waveforms are capable of penetrating walls, foliage, etc., and can gather information about those environments that would normally be hidden [18].

The purpose of this thesis is to utilize the Air Force Institute of Technology (AFIT) noise radar network (NoNet) to explore various NoNet node configurations and image formation techniques that will give rise to optimal target detection and radar imaging. For example, experiments will determine if imaging resolution is finer and target location more accurate depending on the arrangement of the nodes. In addition to node configuration, signal processing techniques will be evaluated. For example, images can be formed with radar data using multilateration and SAR algorithms. Conventionally SAR images have been produced by a direct Fourier reconstruction algorithm. The polar format algorithm is one such algorithm. It and convolution backprojection for SAR will be investigated in this thesis. The analysis of experimental trials will reveal the quality, in terms of image resolution, and computational cost, in terms of execution time, of creating radar images given the various combinations of system configuration and signal processing technique. Results will be weighed against sample requirements to answer whether finer images are desired, or required, or whether a trade off in image quality and computational cost is acceptable in certain scenarios.

1.2 Motivation

Our military has a wide range of sensor assets that provide critical information to warfighters in the battlefield to enhance situational awareness. Assets provide warfighting aids such as communication, precise location and navigation information, missile warning, and imaging. Imaging is certainly a key feature for both warfighters in the middle of the action and military leaders planning and forming strategies from afar.

Optical imaging has limitations that must be overcome. Often, adversaries use the cover of darkness or inclement weather to hide suspicious actions. Whereas optical imagers cannot, radar has the ability produce high quality, high resolution images in this kind of environment. In addition, due to its large bandwidth, random noise radar can be used to produce images of scenes hidden behind walls, foliage, or other similar coverage.

In addition to its through-wall capability, noise waveforms have a low probability of interception (LPI) and low probability of detection (LPD), making them ideal for covert operations in hostile environments. Also, since noise is non-periodic and random, radar receivers can detect only a time-delayed copy of transmitted noise. This property gives noise waveforms an ideal thumbtack ambiguity function making fine range and Doppler resolutions possible. These terms will be discussed in more detail in Chapter 2.

A covert radar system that is invulnerable to jamming or deception and capable of high resolution imaging would be a useful asset in military applications. There are also other possible non-military applications of noise radar imaging. For instance, firefighters could use such a system to determine whether any people or animals are trapped in a burning building, search and rescue teams could canvas a large forest area to locate a downed plane and its passengers, and policemen could evaluate a hostage situation. In all cases, the images created by the radar could be used to determine the best course of action.

The AFIT NoNet was developed in 2009 and has since been shown to effectively detect and image targets using a multilateration imaging technique. Until now, SAR imaging techniques using the AFIT NoNet have been limited and warrants further study.

1.3 Research Goals

AFIT's NoNet has been developed and improved upon over the last several years. Some examples of improvement include the addition of nodes, alternative methods of signal processing, more efficient power use, and research into system miniaturization. In 2009 it was used to demonstrate its capability of through-wall imaging using a multilateration imaging technique. The aims of this research are to expand on the existing multilateral imaging capability of the AFIT NoNet by applying SAR imaging techniques. The node configurations will be used to assess the effect of different configurations of node arrangements on image quality for both multilateral and SAR imaging techniques.

Currently, the AFIT NoNet system consists of radar nodes that, while portable, are not fit for use in a dynamic system. Ultimately, the goal of the research is to provide groundwork for future use of the system as a covertly operating imaging radar in dynamic applications, such as a miniaturized set of NoNet nodes mounted to a formation of unmanned aerial vehicles (UAVs). The goal is achieved by studying the effects of the combination of node configuration and image processing techniques on image quality and banking this information to provide information for future planning and use of the AFIT NoNet as it evolves.

1.4 Thesis Layout

This thesis is organized into five chapters and one appendix.

- Chapter 1 begins with a brief introduction to radar, leading into the problem statement and the motivation for researching noise radar imaging. The research goals are stated and this thesis layout overview is provided.
- Chapter 2 provides an introduction and background to noise radar, including basics behind transmission, reception, and processing of noise radar waveforms. The function of the AFIT NoNet system is also discussed. Finally, radar imaging is discussed, including the multilateration and SAR imaging techniques.
- Chapter 3 describes the methodology, including the processes and procedures required to accomplish this research. The parameters, configuration, and imaging techniques of each experiment are detailed. The application of the theory discussed in Chapter 2 is the basis for experimental design and methodology.
- Chapter 4 captures the results of the experiments and subsequent processing. The results are analyzed and assessed based on image quality (resolution) and computational expense.

- Chapter 5 reports the conclusions and discusses possible recommendations for future research on the AFIT NoNet.
- Appendix A contains the Matlab codes used to process and form images from the collected radar data

II. Theory and Background

The aim of Chapter 2 is to provide the theory behind noise radar and SAR imaging. Section 2.1 presents the basic concepts in transmitting and receiving random noise signals, then the background of the AFIT NoNet system is discussed. Section 2.2 explains the radar imaging techniques employed in this research; multilateration, polar format, and convolution backprojection. It has been shown that the AFIT NoNet can be used to produce scene images using multilateration. The aim of this research is to apply other imaging algorithms using the noise radar that yield higher quality images than those produced by multilateration.

2.1 Noise Radar

The earliest research in noise radar was developed over 50 years ago, but proceeded slowly due to immature radar hardware and technological barriers [13]. Since then, technological advances in electronic components and signal processing techniques have been made that can handle the complexity and volume of noise radar data. Utilizing research and construction of a noise radar system developed at Pennsylvania State University [12], AFIT students created the AFIT NoNet in 2009 [18]. This section discusses basic noise radar technology and introduces the AFIT NoNet.

2.1.1 Noise Radar Characteristics.

Rather than using conventional radar signals such as pulses, sinusoids, LFM, or phase/frequency coded waveforms, noise radar uses a random noise waveform. The random property of the transmit signals give noise radars many advantages over conventional systems that use pulses or deterministic waveforms. Some of these advantages are unambiguous measurement of range and Doppler estimations, LPI, LPD, electronic counter countermeasure (ECCM), and an ideal thumbtack ambiguity function leading to

fine range and Doppler resolutions [20]. The following describes how these characteristics relate to noise waveforms.

Conventional pulsed radar systems experience range ambiguity due to the repeating structure of transmit waveforms and the manner of reception. Range ambiguities happen because these types of systems have distinct periodic transmit times and listening times. A return echo from a distant target that is received after a subsequent pulse(s) has already been transmitted will look like a return echo from a target which is close, when in fact the receiver is detecting an echo from a previous pulse. In a pulsed radar system, the maximum range that a target can be detected before transmission of the next pulse is called the maximum unambiguous range [16]. Noise radars use a continuous wave (CW) noise waveform that is truly random and never repeats. Any two samples of a CW noise waveform are unique. For this reason noise radar systems are capable of unambiguous range measurement.

Deterministic radar waveforms can easily be detected by passive radar receivers. LPI and LPD are characteristics of noise waveforms that make noise radar attractive for covert use. In order for a radar receiver to detect targets, it must know what kind of radar signal was transmitted to interrogate the scene of interest. Since noise radars transmit noise, the radar receiver must expect noise. However, it is not enough to simply expect noise; the receiver needs to know exactly what noise to expect. As mentioned above, any sample of noise is unique when compared to other samples. Any radar receiver without the prior knowledge of the transmitted waveform will simply detect noise, which occurs naturally; thus, noise radars have LPI and LPD. In Section 2.1.3 the noise radar receiver will be discussed in more detail.

Electronic counter measures (ECMs) are measures taken to deceive (create false targets) or jam (conceal real targets) radar systems. Noise radars have good defense against ECMs, referred to as ECCM. To hide targets, an ECM would be to introduce noise, thus

lowering the signal to noise ratio (SNR). Since noise waveforms have UWB with power uniformly spread throughout its frequency band, spot jammers, or jammers which target specific frequencies, are ineffective. Barrage jamming, which targets multiple frequencies, or bands of frequencies, must spread their transmit power over these frequency bands. As the bandwidth increases, the power attacking each frequency decreases, which lessens a barrage jammer's effect. As such, UWB signals have good defense over barrage jamming. The noise waveform's UWB property will be discussed further in Section 2.1.2. In order to deceive a radar into detecting a false target, the jamming radar must send a waveform that is matched to the radar receiver. Noise radar receivers operate by using a sampled copy of the transmission signal, which is continuously and randomly generated in the transmitter chain. It is impossible for a radar outside of the noise radar system to generate the correct waveform.

Noise waveforms also have an ideal thumbtack ambiguity function and can achieve fine range and Doppler resolutions. The ambiguity function represents the time response of a filter matched to a given finite energy signal when the signal is received with a delay τ and a Doppler shift f_d relative to the nominal values (zeros) expected by the filter and is given by

$$|\chi(\tau, f_d)| = \left| \int_{-\infty}^{\infty} u(t)u^*(t + \tau)e^{j2\pi f_d t} dt \right|, \quad (2.1)$$

where u is the complex envelope of the signal [10]. The integral operation in Equation (2.1) is the matched filter response [10]. The ambiguity function is a signal analysis tool used to evaluate ambiguities due to a signal return on the matched filter and reveals trade-offs in range or Doppler measurements [10]. An ideal ambiguity function will feature single sharp peak at the origin, like a thumbtack. Figure 2.1 shows the ambiguity function of a pseudo-random noise signal created in Matlab. It shows a sharp peak at the origin that indicates that a noise radar receiver is ideally matched to the transmitted signal and achieves high range and Doppler resolution.

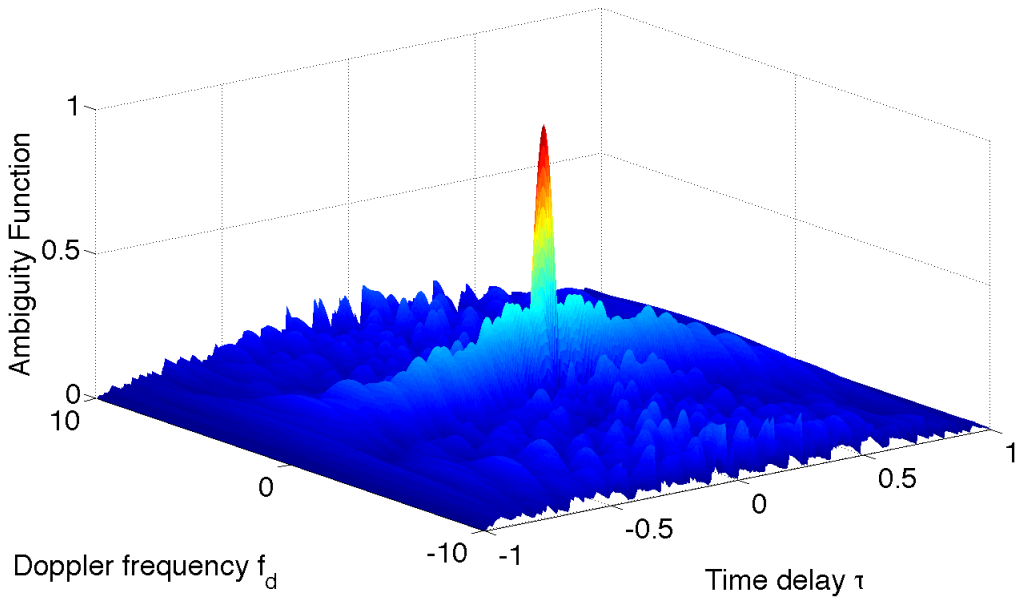


Figure 2.1: The ambiguity function of a pseudo-random noise signal created in Matlab. Noise signals have a thumbtack ambiguity function and are capable of achieving high range and Doppler resolution.

With LPI and LPD coupled with good ECCM, noise radars are appealing for military use. In addition to their inherent covert characteristics, noise waveforms have an ideal thumbtack ambiguity function and can achieve high range and Doppler resolution. The following section discusses aspects relating to the transmission and reception of noise radar signals.

2.1.2 Noise Radar Transmission.

As its name suggests, noise radars make use of a noise waveform as a transmitted signal. Noise signals can originate from an analog source, such as thermal noise generated from an amplified noise diode, or can be created digitally. Digitally created noise is known as pseudo-random noise. The noise waveforms employed by the radar systems

are generally white and Gaussian, that is, the waveform's power spectral density is uniform over all frequencies contained in the waveform [9].

Due to its random nature, white Gaussian noise (WGN) samples are independent and identically distributed (IID), meaning any two WGN signals are orthogonal and uncorrelated [9]. Another inherent property of noise is its wide bandwidth. In theory random noise contains all frequencies and has infinite bandwidth, however, in practice, random noise signals will be bandlimited due to hardware constraints [14].

Due to the wide bandwidths of noise radar systems, they are classified as UWB systems. According to IEEE and the US Defense Advanced Research Project Agency, UWB radar systems are characterized by transmission waveforms that have a fractional bandwidth of at least 25%. The fractional bandwidth, B_f of a signal is given by [14],[19]

$$B_f = 2 \frac{f_h - f_l}{f_h + f_l} \quad (2.2)$$

where f_h is the signal's highest frequency and f_l is the lowest frequency.

For a monostatic radar, the resolution, or the radar's ability to distinguish between two closely spaced targets, is proportional to the ratio of the speed of propagation of the transmission signal and the bandwidth [16]. Since radars use two-way propagation, a factor of 2 enters the equation. The range resolution, ρ_r is given by

$$\rho_r = \frac{c}{2B} \quad (2.3)$$

where c is the speed of light (speed of propagation in free space) and B is the transmission signal bandwidth. The UWB property of noise signals results in fine resolution.

In 2D radar imaging, the cross-range is the dimension perpendicular to the range. This dimension also has a resolution, called the cross-range resolution, and will be defined and discussed in Section 2.2.2.

2.1.3 Noise Radar Correlation Receiver.

Rather than processing received signals with matched filtering or some other conventional radar processing method, noise radar uses a correlation receiver. This type of receiver uses a delayed copy of the transmit signal and performs a cross-correlation with actual received echoes. Ideally, the value of the cross-correlation peaks when the delayed copy and echo align and is zero elsewhere due to orthogonality. The time delay corresponds to the roundtrip time of the signal and is a measure of distance to the target. This section explains the correlation receiver in more detail.

The following development is taken from [20] with elements from [9]. If $x(t)$ and $y(t)$ are the transmitted and received signals of a radar system and r_0 is the range to a point scatterer, the received signal can be written as

$$y(t) = Ax(t - T_0) \quad (2.4)$$

where

$$T_0 = 2r_0/c \quad (2.5)$$

is the round trip time delay of the electromagnetic transmit signal traveling at the speed of light and A corresponds to the reflectivity of the target. In this derivation you can assume that $A = 1$ without loss of generality. The matched filter result of the the transmitted and received signals is given by

$$R(\tau) = \int_0^{T_{int}} y(t)x^*(t - \tau)dt \quad (2.6)$$

where T_{int} is the integration time. We will show that Equation (2.6) has a maximum value at time $\tau = T_0$ when the transmit signal $x(t)$ is a random noise waveform.

In a noise radar, $x(t)$ is a WGN random process with an autocorrelation function $R_{xx}(\tau)$. The received signal, $y(t)$, is simply a time delayed version of the transmitted signal and is therefore also a random process. The matched filter output of $x(t)$ and $y(t)$ must also be a

random process [9]. The expected value of the matched filter output is [20]

$$\begin{aligned}
E[R(\tau)] &= E \left[\int_0^{T_{int}} y(t)x^*(t - \tau)dt \right] \\
&= \int_0^{T_{int}} E[y(t)x^*(t - \tau)] dt \\
&= \int_0^{T_{int}} E[x(t - T_0)x^*(t - \tau)] dt \\
&= \int_0^{T_{int}} R_{xx}(\tau - T_0)dt \\
&= T_{int}R_{xx}(\tau - T_0).
\end{aligned} \tag{2.7}$$

The auto-correlation, R_{xx} , is maximum when $\tau - T_0 = 0$, or when $\tau = T_0$. The correlation peaks at the maximum expected value of Equation (2.7) when $\tau = T_0$.

2.1.4 AFIT NoNet (Noise Network).

The AFIT NoNet was first developed in 2009 where it was shown that a system of multiple radar nodes could be used to detect targets through a wall and produce images using a multilateration technique [18]. The system has since been studied for other uses, such as indoor navigation in [22], and for upgrades, such as system miniaturization in [11] and improvements to system performance in [5]. The NoNet currently consists of six individual radar nodes that can be networked and used in a monostatic, netted monostatic, or multistatic configuration. In the netted monostatic configuration, the system of nodes is networked and each node works simultaneously, but only as a monostatic radar node. In the multistatic configuration, the system of nodes is also networked and operate simultaneously; however, each node may operate both monostatically and as a bistatic pair with each of the other nodes. In this research, a single node is utilized in the monostatic configuration; however, the netted monostatic configuration is simulated in the method of signal processing.

Figure 2.2 shows a NoNet radar node. Technically, the transmit and receive antennas are separate, constituting a bistatic configuration. However, since the antennas are so close

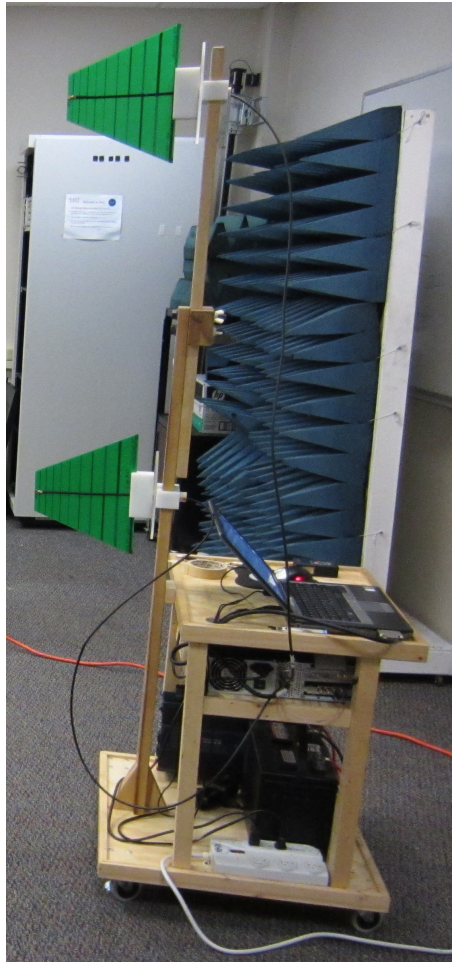


Figure 2.2: A NoNet radar node. Each node consists of a computer, noise radar box, transmit and receive antennas, and a battery power source (note an AC power source may also be used).

together, the nodes can be approximated as CW monostatic radars. Using the theory and principles discussed in Section 2.1.2, the AFIT NoNet node transmits and stores random CW noise signals generated from an amplified thermal noise diode connected to the transmitter. The received signal is sampled, digitized, and then processed with the stored transmit signal using a correlation receiver as discussed in Section 2.1.3. Figure 2.3 shows the block diagram of a NoNet node.

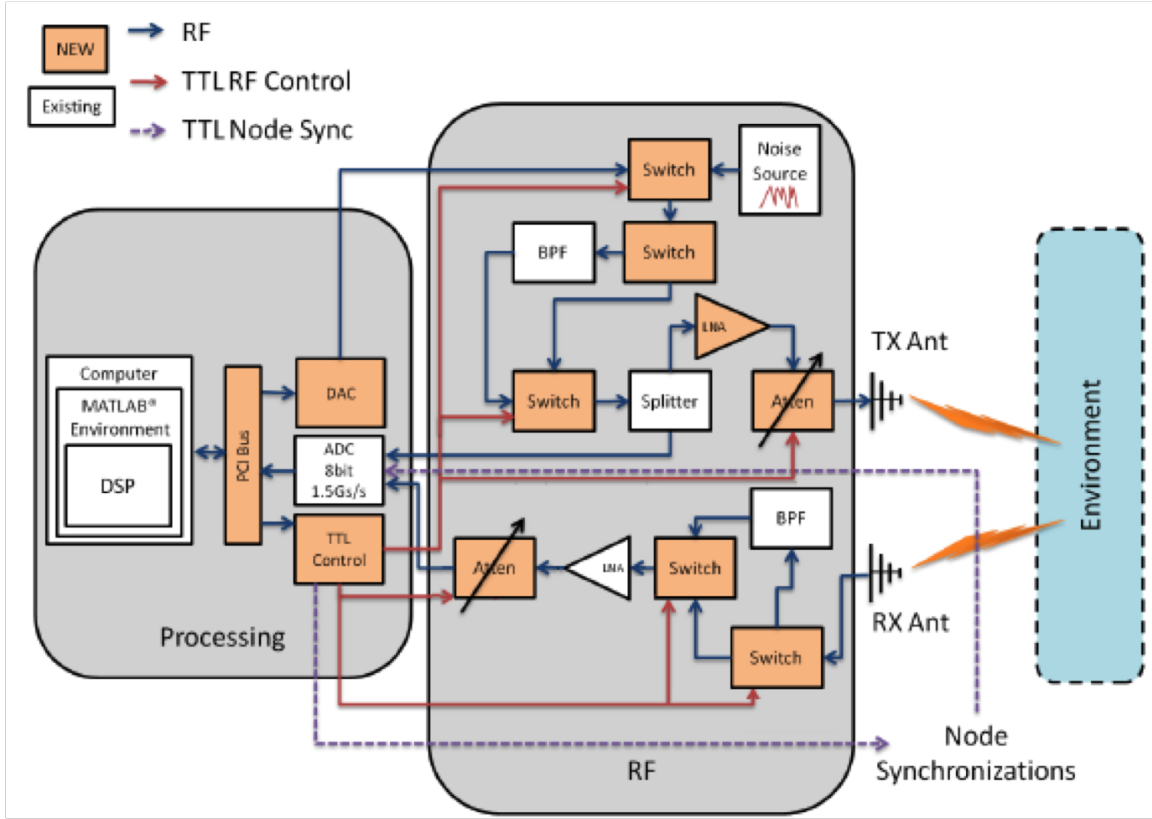


Figure 2.3: Block diagram of AFIT NoNet.

Taken from real collected data, Figure 2.4 shows a raw transmission signal from a NoNet node. The histogram of the signal, shown in Figure 2.5, shows that the signal has a Gaussian distribution as discussed above. For the best system performance and detection of the transmission signal, it is important that the received signal keeps the Gaussian distribution and is within the dynamic range of the receive analog to digital (A/D) converter.

If and when the received signal saturates, the property of Gaussian distribution is lost and, although there may still be a degree of correlation with the transmitted signal, correlation is greatly degraded. The NoNet contains hardware, such as bandpass filters and attenuators on both the transmit and receive sides, that can be toggled using controls in the

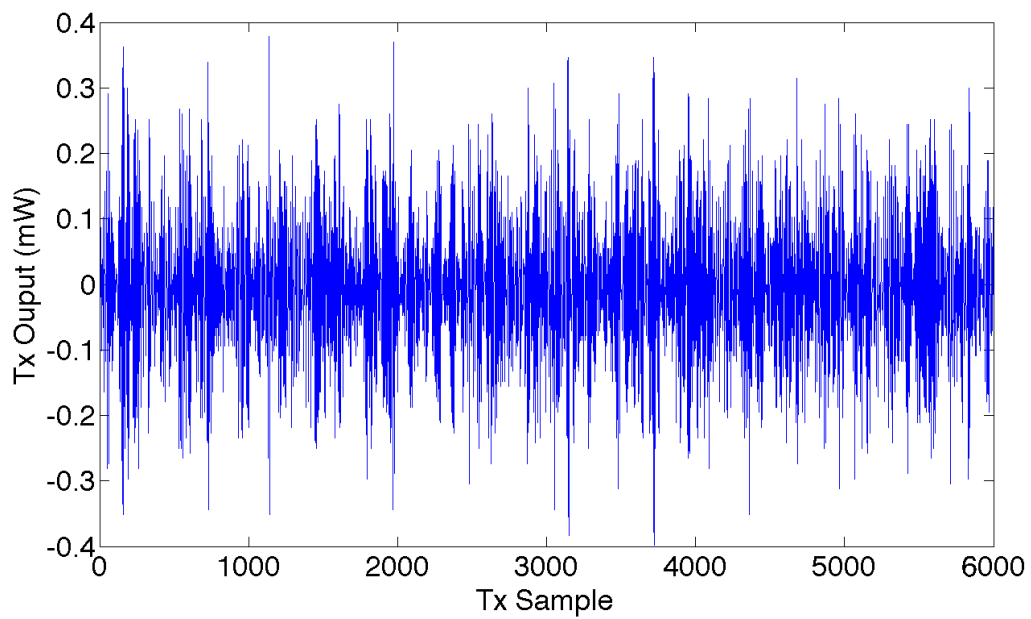


Figure 2.4: A sample of the raw transmitted noise waveform.

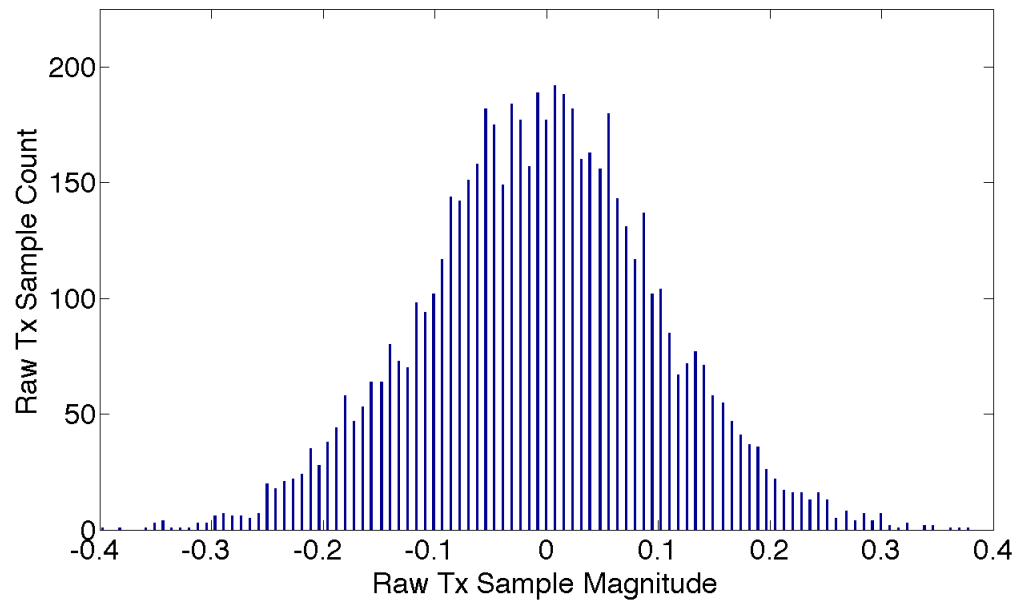


Figure 2.5: Histogram of the transmission signal shown in Figure 2.4. The histogram shows that the signal has a Gaussian distribution.

NoNet software. These controls are important for maintaining the Gaussian distribution in the received radar signals. The raw received signal resulting from the collection of the data transmitted in Figure 2.4 is shown in Figure 2.6 and its histogram in Figure 2.7. The figures show that the integrity of the Gaussian distribution in the received signal is preserved.

One can see from Figure 2.2, the radar node is equipped with log-periodic antennas capable of transmitting wide bandwidth signals. As mentioned above, the NoNet contains bandpass filters on both the transmit and receive sides. Figure 2.8 shows the spectrum of the transmitted signal shown in Figure 2.4. This spectrum is representative of any transmitted signals spectrum. Figure 2.8 shows that the theoretically infinite bandwidth noise signal is bandlimited by the hardware filters to approximately 450 MHz, ranging from about 350 to 800 MHz. From Equation (2.2) the fractional bandwidth of the NoNet radar is

$$B_f = \frac{(800 - 350)\text{MHz}}{(800 + 350)\text{MHz}} \\ = 0.783, \quad (2.8)$$

well over the required 25% for an UWB signal.

2.2 Radar Imaging

Radar imaging uses conventional radar data and attempts to create an image of the scene by mapping the intensity of the received signal onto an image plane (or image space in the 3D case). Scatterers in a radar scene reflect energy back to the radar, the strength of which depends on several factors including radar cross section (RCS), orientation, and material makeup. A single monostatic radar at some position collects only range and Doppler information, which makes 2D imaging impossible unless data of the scene is collected from multiple spatially distributed radar sensors or a synthetic aperture is created by using multiple radar sensors or by moving a radar sensor.

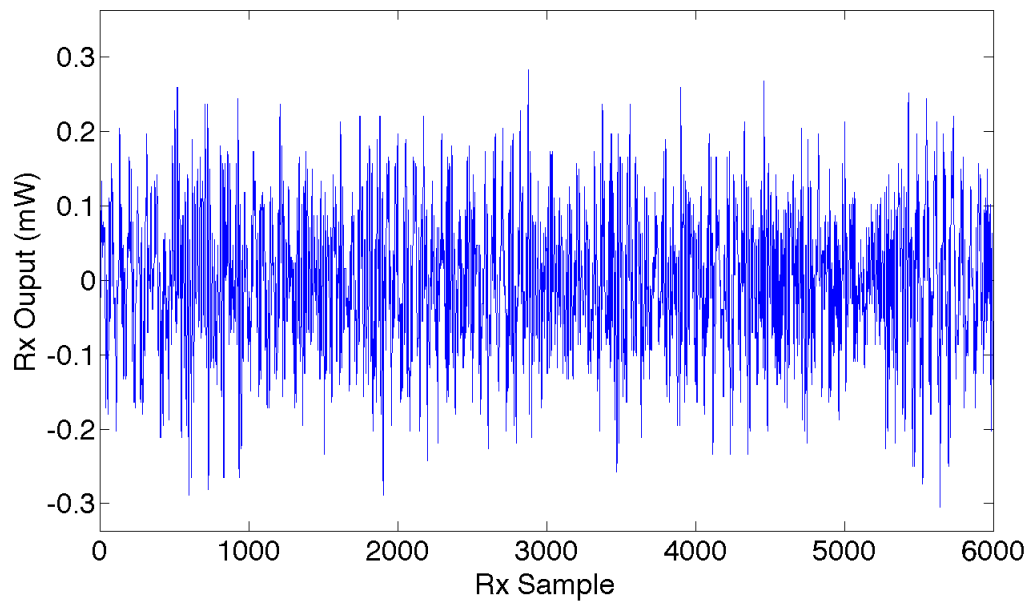


Figure 2.6: The raw received waveform from the transmitted signal shown in Figure 2.4.

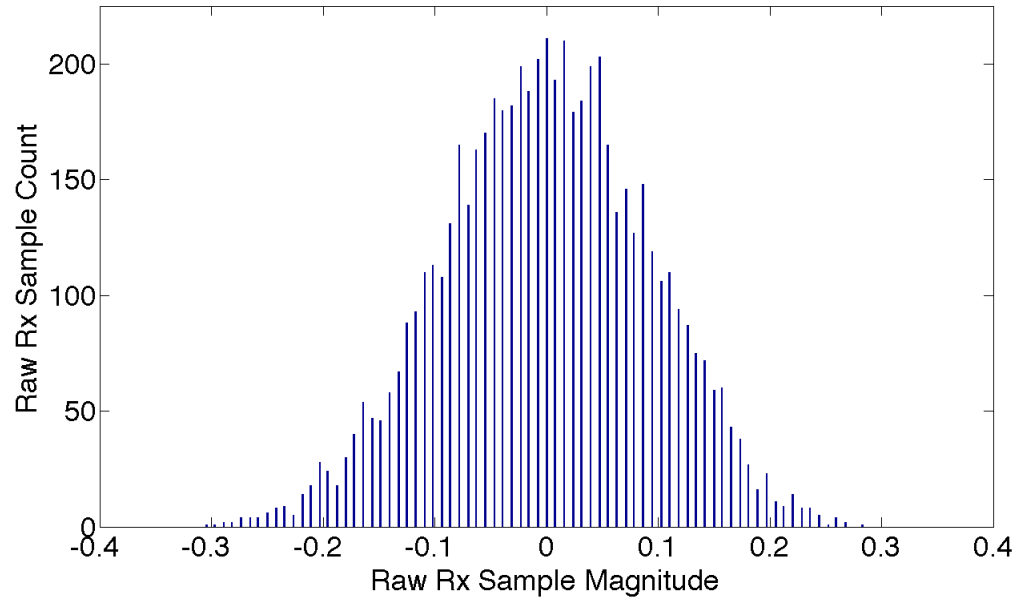


Figure 2.7: Histogram of the received signal shown in Figure 2.6. The histogram shows that the received signal kept Gaussian distribution.

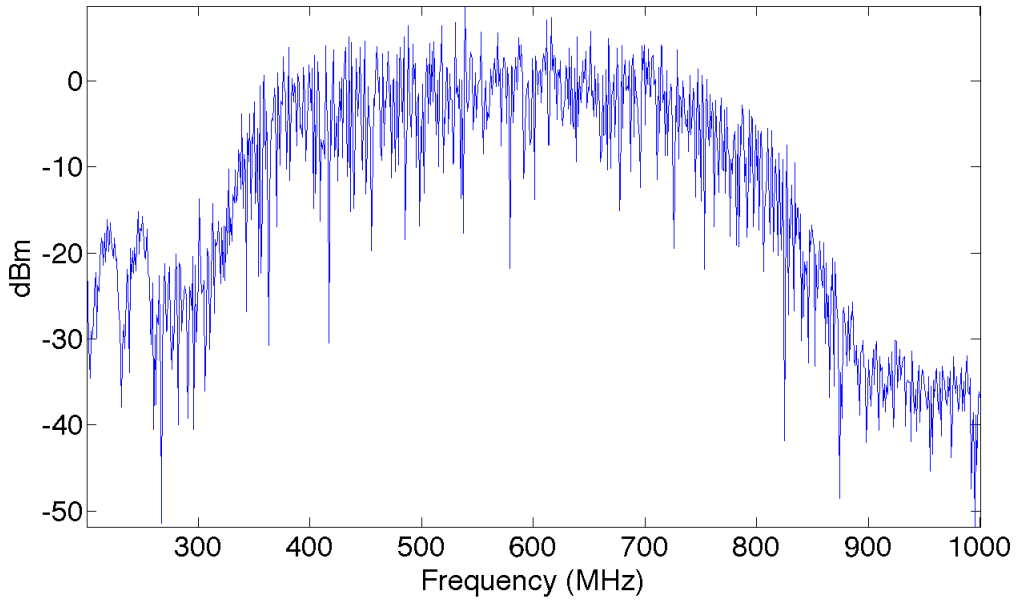


Figure 2.8: The frequency spectrum of the transmitted signal shown in Figure 2.4.

The AFIT NoNet has been shown in [14] and [18] to effectively locate targets using a network of nodes and create 2D images using a multilateration imaging technique. Multilateration imaging uses purely range data to locate a target much like navigation systems such as global positioning system (GPS) does. However, even with multiple, spatially distributed nodes, image quality may suffer from degraded resolution and artifacts such as smearing and ghosting. The relationship between resolution and the spatial distribution of the radar nodes will be discussed in further detail in Section 2.2.1.

SAR provides the capability to generate high resolution images by creating a synthetic aperture sensor movement along some path or combining the data from multiple spatially distributed radar sensors. By creating a synthetic aperture a SAR system can create an image in 2 dimensions: range and cross-range. SAR synthesizes a large antenna by moving a small antenna along some path for some distance. Range is defined as the dimension perpendicular to the path of the SAR antenna and cross-range is the dimension along the

SAR antenna's path. The synthesis of a large antenna for SAR and its range and cross-range resolutions is discussed in more detail in Section 2.2.2. The subsections Section 2.2.2.1 and Section 2.2.2.2 discuss the polar format and convolution backprojection SAR imaging techniques. Until now, use of SAR imaging techniques using the AFIT NoNet have been limited and warrants further study.

2.2.1 Multilateration Imaging.

Multilateration is a technique which uses the range information of a network of sensors to pinpoint the location of a target. In radar, the distance to a target can easily be obtained using the two-way propagation time given by Equation (2.5), $T_0 = 2r_0/c$. Unfortunately, a single monostatic radar only collects range data in one dimension. With at least 3 known spatially distributed sensors it is possible to extract the 2D position of the target by linearly combining their data [18].

Multilateration projects the range data from multiple sensors onto a 2D space. Each sensor will have a unique range profile depending on its location relative to the target. Generally, the range profile should have its max intensity at a position corresponding to the range of the target. The linear combination of each sensor's image will produce an overall image whose intensity is greatest where the range profiles intersect. In this research, all radar nodes operate in a monostatic configuration, therefore range contours will be perfect circles.

A multilateration system requires at least three sensors to localize a target. This can be imagined by first considering a system with two sensors detecting a target. The range profiles of the two sensors will form circular contours on the image. The intersection of the circles will indicate where the target is; however with only two sensors, the circles will overlap at two locations. A third sensor is required to distinguish between the real target and where the range contours happen to overlap due to the spatial distribution of the

original two nodes. In a system, target ghosts, or false targets, are targets that are detected at the intersection of range contours where no target is actually present.

Since multilateration simply sums the range profiles, the monostatic range resolution is also the finest possible resolution achievable in cross-range. The smallest range and cross-range resolution cell is formed by two distributed monostatic range measurements that are spatially orthogonal with respect to a resolution cell containing the target of interest [14]. Since localization of a target requires at least three sensors, if the location of the third sensor is not 180° from either of the two other sensors, the target resolution will degrade.

Figure 2.9 shows an example of multilateration imaging using a 1×4 (one transmitter/four receiver) configuration [14]. Though this configuration uses 3 bistatic radar pairs and 1 monostatic radar, the concept is the same. One can see from the figure that the target is indicated by the location of highest intensity. It was previously mentioned that the highest resolution cell is formed by two monostatic range contours that are spatially orthogonal to the cell. You can see from Figure 2.9 that since this is not true, there is some smearing and degradation of the resolution where the range contours intersect.

Unfortunately, for multistatic imaging, depending on the configuration of the radar sensors, target smearing and/or ghosting can occur, degrading the image resolution and/or creating false targets. Target ghosts are the result of the

The multilateration method does not use any phase history data or Fourier theory and is very computationally inexpensive making it a candidate for real-time or near real-time applications, should image quality suffice. Additionally, since data is collected and processed in the time domain with real valued data, there is no reason to sample in the Fourier domain, thus multilateration imaging does not suffer from aliasing. It may, however, suffer from target ghosting. The multilateration imaging algorithm will be discussed in more detail in Section 3.3.1.

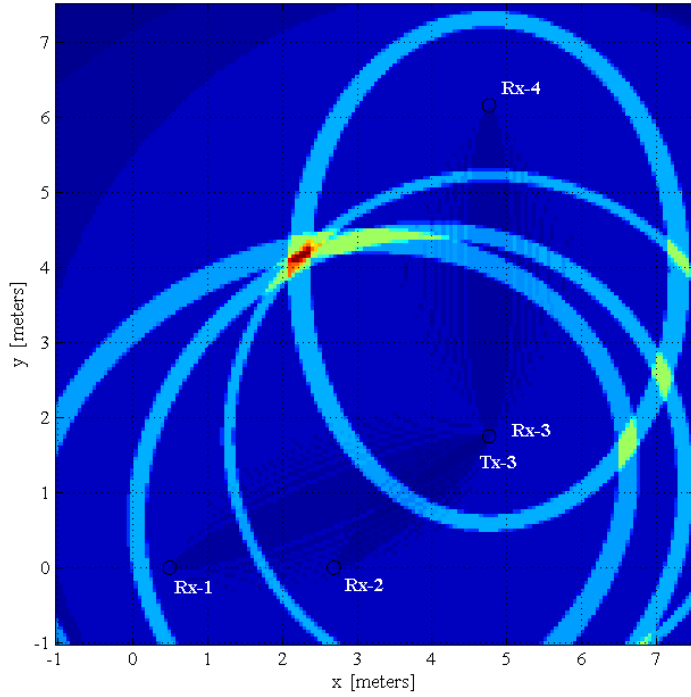


Figure 2.9: Example of a 1×4 (one transmitter/four receiver) multistatic location estimate using multilateration of isorange contours for target position (reproduced from [14]).

2.2.2 Synthetic Aperture Radar (SAR) Imaging.

SAR is an imaging system that came about with the desire to improve image resolution. The method is mainly exploited for improving the azimuth resolution of radar images by synthesizing a large antenna aperture by moving a small antenna along a path [1]. Typically SARs produce images in two dimensions, generally called the range and cross-range.

For a side looking SAR, the dimension perpendicular to the path that the sensor moves along is considered the range direction. Range measurements and resolution for SAR systems are computed the same way as conventional radars. That is, range is governed

by Equation (2.5), rewritten as $r_0 = cT_0/2$, and the range resolution is governed by Equation (2.3).

The azimuth, or cross-range, is the dimension perpendicular to range, along the SAR sensor's path. The cross-range resolution of an antenna is related to its half-power beam width. The half-power beam width, $\beta = \lambda/L$ [1] and the cross-range resolution is ρ_x scaled by κ [6]

$$\rho_x = \frac{\kappa\lambda}{L}, \quad (2.9)$$

which depends on both the wavelength, λ , and the physical length, L , of the antenna. To realize fine cross-range resolution a physically large antenna is required to focus the transmitted and received signals into a narrow beam. The narrower the beam, the finer the resolution. A long synthetic aperture synthesizes a narrow synthetic beam width, thereby improving the resolution. The beam forming can be explained in terms of a phased array antenna.

SAR is similar to a phased array antenna that uses antenna elements that are spatially distributed in a line. Each element has the same radiation pattern; however, the collective radiation pattern of the all elements is the pattern of a single element multiplied by an array factor [1]. The radiation pattern of the array has a much narrower beamwidth than that of a single element. When the transmitted signal interacts with scatterers in the scene, an echo is returned. The returned signal from any scatterer will have spherical wavefronts; however, a linear array only senses a circular wavefront (1D). The circular wavefront causes each element in the phased array to receive the signal at a slightly different phase. Though each element detects a slightly different phase, they have the same reference phase, thus the received signals have phase coherence [16]. Both amplitude and phase history should be stored. If the stored phase history has phase coherence, the phase history can be used to locate the where in the scene an echo return originated from.

SAR differs from a phased array antenna in that it uses a single antenna and, by moving along a line, collects data from spatially distributed positions. At each position the return signal amplitude and, importantly, phase are stored. After the antenna has moved over some desired length, L_{syn} , the collection of data, including the phase history, resembles that which would have been collected by an actual linear array [1] (that is, similar to the phased array antenna of length L as described above).

Unfortunately, to achieve even a moderate cross-range resolution requires prohibitively large physical antennas. For example, if you have a radar that is operating at 10 GHz with the scaling factor $\kappa = 65$ (a typical scaling factor) and a resolution of 0.1 m is required, one would need an antenna that is 19.5 m long [6]. SAR avoids this need by creating a synthetic aperture using a physically small antenna.

For SAR, the aperture extent, or the total azimuth angle, determines the cross-range resolution. The cross-range resolution, ρ_x is given by [8]

$$\rho_x = \frac{\lambda_c}{2\Delta\phi}, \quad (2.10)$$

where λ_c is the center wavelength of the signal and $\Delta\phi$ is the aperture extent.

Since SAR imaging requires use of the phase history domain data, the rate at which the data is sampled determines whether there will be aliasing in the spatial domain. The alias free range extent, W_r , is inversely related to the frequency sampling rate, Δf . The alias free cross-range extent, W_x , is related to the sampling rate across the synthetic aperture, or the azimuth spacing $\delta\phi$. W_r and W_x are given by [8]

$$W_r = \frac{c}{2\Delta f} \quad (2.11)$$

$$W_x = \frac{\lambda_{min}}{2\delta\phi} \quad (2.12)$$

In this research spotlight mode SAR is used. In spotlight mode SAR the transmit antenna is steered to illuminate the same scene patch from any sensor position. Two imaging techniques are used to produce SAR images; convolution backprojection and polar

format. Conventionally SAR images have been produced by a direct Fourier reconstruction algorithm. Polar Format is one such algorithm. Here we also study the use of convolution backprojection.

2.2.2.1 Polar Format Imaging.

Polar format imaging is a conventional direct Fourier method that uses a reconstruction algorithm based on the 2D inverse fast Fourier transform (IFFT) [8]. The method has two major setbacks. First, use of the IFFT requires that all data must be recorded before image processing can begin. Second, since data is recorded on a polar raster, interpolation to a Cartesian raster is required before the 2D IFFT can be performed. The interpolation is relatively computationally expensive and prone to errors due to inaccuracies, especially as the synthetic aperture extent gets longer [2].

Along the radar line of sight (LOS), the phase history data is recorded on a polar raster as shown in Figure 2.10 [6]. The data falls on polar raster because of the geometry of spotlight SAR. In spotlight SAR the radar is steered to illuminate the same scene with the same center from any position along the synthetic aperture. The figure shows that the phase data samples are not equally spaced in x and y , or on a Cartesian grid. In the case of the AFIT NoNet, the data from each node, or look angle, is a range profile that must first be converted to a phase history by taking a fast Fourier transform (FFT). The Fourier data, now on a polar grid, must be interpolated onto a Cartesian grid. Interpolation is accomplished by first interpolating in the range direction, which results in the data lying on a keystone grid. Then, interpolation is applied in the azimuth direction, which results in the data lying on a rectangular Cartesian grid [3]. Figure 2.11 illustrates the interpolation process [6]. Finally, the image can be constructed by simply taking the 2D IFFT of the interpolated data.

As mentioned earlier, a drawback of the polar format algorithm is that it requires interpolation of data on a polar grid to a Cartesian. From Figure 2.10 you can see that

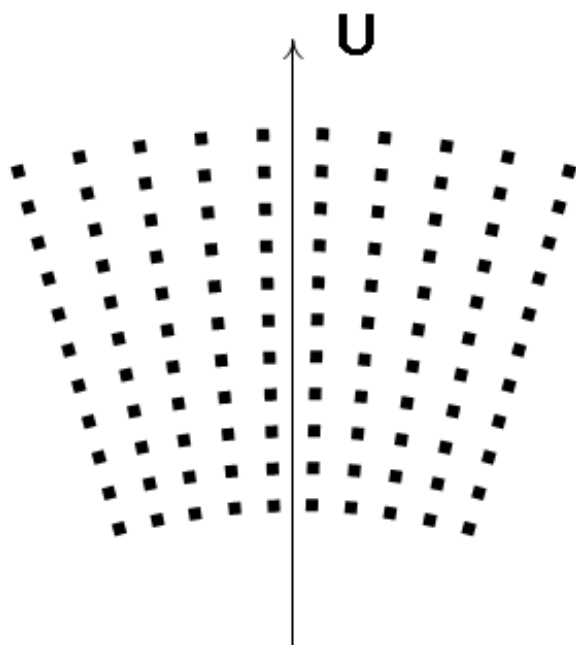


Figure 2.10: A representation of phase history of a spotlight SAR system

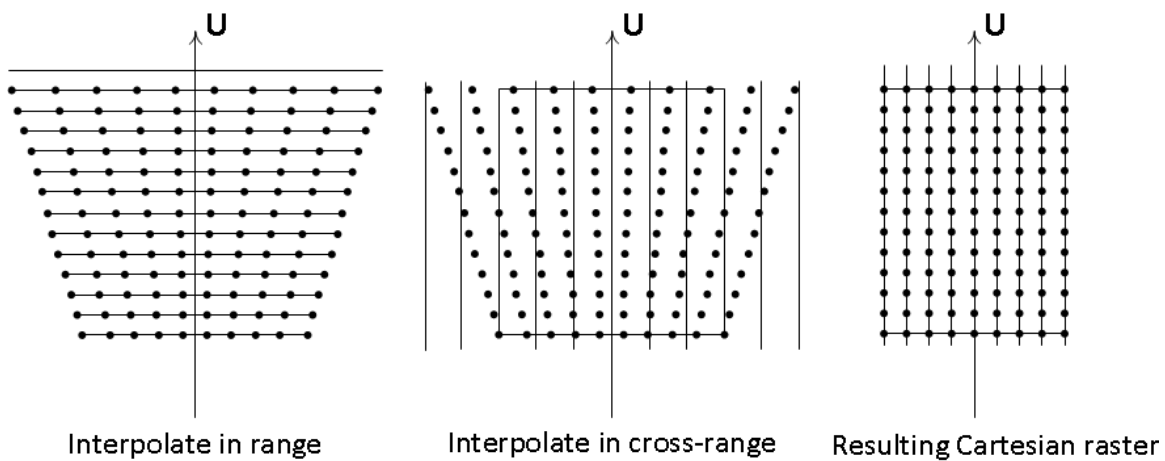


Figure 2.11: Illustration of interpolation from polar to Cartesian raster

along the radial direction, the data are sampled evenly. The data are also sampled evenly in azimuth. However, because the data is on a polar grid, the samples closer to the polar

origin are closer together. Interpolation to a Cartesian grid inscribes a rectangle around the phase data and moves the points onto the Cartesian grid. The quality of the interpolator dictates the accuracy of the transformation. In any case the polar data will not lie exactly on a Cartesian grid, thus interpolation introduces some error. This can be visualized by picturing a rectangular grid with equal spacing in the x and y directions over the data representation in Figure 2.10. Depending on how fine the Cartesian grid is, you can imagine that not all points lie on the Cartesian grid, thus some error is introduced. At small azimuth angles, the phase history data is approximately a rectangle, and interpolation works well. As the azimuth angle increases, more error can be introduced because the data resembles an annular ring, on which a rectangle does not fit as closely.

Despite the drawbacks mentioned above, the polar format imaging algorithm is straight forward and relatively computationally inexpensive. The complexity of the algorithm is $P(N) + O(N^2 \log_2 N)$, where N is the number of pixels in each dimension, $P(N)$ is the computational complexity of the interpolator and $O(N^2 \log_2 N)$ is the computational complexity of the 2D IFFT [2].

2.2.2.2 Convolution Backprojection Imaging.

Convolution backprojection is a method that is able to use the data directly from the radar sensor. Specifically, it can perform its operations on the data sampled on the polar raster. Because no interpolation is required, there is no loss of data and backprojection can produce higher quality images.

Though it was not explicitly stated above, the data that SAR systems collect are line integrals, or projections, from various look angles. In other words, the 1D range profile data from each look angle, ϕ , is a projection of the scene onto a range line and is therefore the Radon transform of the scene along ϕ . The Radon transform along angle ϕ , $g_p(u, \phi)$, of

a reflectivity function, $g(x, y)$ is given by [7]

$$g(u, \phi) = \int \int_{-\infty}^{\infty} g(x, y) \delta(x \cos \phi + y \sin \phi - u) dx dy \quad (2.13)$$

$$= \int_{-\infty}^{\infty} g(u \cos \phi v \sin \phi, u \sin \phi + v \cos \phi) dv. \quad (2.14)$$

In Equation (2.13) the variable u is range. The Fourier transform of $g_p(u, \phi)$ is $G_p(U, \phi)$.

Convolution Backprojection uses a form of the inverse Radon transform to reform the image from the collection of projections. The reflectivity function of the scene, $g(x, y)$ (which gives the image), is related to its spatial frequency domain data by [6]

$$g(x, y) = \int \int_{-\infty}^{\infty} G(U_x, U_y) e^{j2\pi(U_x x + U_y y)} dU_x dU_y \quad (2.15)$$

$$= \int_0^{\pi} \int_{-\infty}^{\infty} |U| G_{polar}(U, \phi) e^{j2\pi U(x \cos \phi + y \sin \phi)} dU d\phi, \quad (2.16)$$

where, in Equation (2.16) the upper limit of integration on the outer integral was changed and $g(x, y)$ was converted to polar coordinates with $|U|$ being the Jacobian [2]. The spatial frequency domain, also referred to as the phase history domain, is analogous to the frequency domain for functions of time. An image plane intensity distribution is composed of spatial frequencies in the same way that a time domain function is composed of various frequencies. The relationship between the image plane intensity distribution and the spatial frequency domain can be analyzed using Fourier analysis (Equation (2.15) is a 2D inverse Fourier transform).

By the projection slice theorem G_{polar} can be replaced with the Fourier transform of the Radon transform. The convolution backprojection reconstruction equation then becomes

$$g(x, y) = \int_0^{\pi} \int_{-\infty}^{\infty} |U| G_p(U, \phi) e^{j2\pi U(x \cos \phi + y \sin \phi)} dU d\phi. \quad (2.17)$$

The inner integral on U in the spatial frequency domain is equivalent to an inverse Fourier transform. In the spatial domain this translates to a convolution of the projections $g_p(u, \phi)$ with a filter whose frequency response is the inverse Fourier transform of $|U|$.

Generally the convolution is applied as multiplication in the spatial frequency domain because convolution is more computationally complex than performing a multiplication. Thus, the inner integral is the collection of filtered projections. The outer integral is the backprojection operation used to sum the contributions of the projections and reform the image [6].

The convolution backprojection algorithm has a complexity of $O(N^3)$ for an $N \times N$ image, an order of magnitude higher than that of polar format [2]. However, unlike polar format, the backprojection algorithm can process data as it is collected.

2.3 Chapter Conclusion

The AFIT NoNet uses noise radar technology to interrogate and collect data from the area of interest. Among other things, it has been used to detect targets and produce 2D images using a multilateration technique. This research aims to expand on the imaging capability by applying SAR imaging algorithms. Two types of SAR algorithms are used: polar format algorithm and convolution backprojection algorithm. Though both should offer improved cross-range resolution by synthesizing a large aperture, each has its advantages and disadvantages. The polar format algorithm requires interpolation of phase history data from a polar to Cartesian grid which introduces error. The error is amplified the longer the aperture synthesized. However following interpolation, the image is readily constructed with a simple 2D IFFT. The convolution backprojection algorithm is able to process data as it is collected without having to perform any interpolation; however, it is more computationally complex and takes longer to process.

III. Methodology

Chapter 3 describes the methodology and procedures used to conduct meaningful experiments. The experiments consist of the application of the imaging algorithms using real world data collects. Section 3.1 describes how the NoNet was used to collect data, and Section 3.2 describes the 4 NoNet configurations used and the logic behind the design. In Section 3.3 the imaging, resolution measuring, and algorithm timing techniques are discussed.

3.1 Data Collection Parameters and Method

AFIT's NoNet was designed to allow a user to configure many parameters including run time, number of triggers per acquisition, sampling rate, signal attenuation levels, use of hardware filters, and the acquisition mode. For consistency, the same parameters, shown later in Table 3.1, were used for each experiment, with the exception of one parameter. In one configuration, the number triggers per acquisition differed and will be discussed in Section 3.2.1.

The node arrangements designed for experiments simulate the use of AFIT NoNet nodes working in a netted monostatic configuration. That is, each node is geographically separated, but data from each node is considered as having been collected concurrently. For consistency of operating characteristics between all measurements, a single node, NoNet-4, was used for all data collections by physically repositioning the node for each measurement.

For a configuration of geographically separated radar sensors, the returns from a target may look different depending on the target's shape and and the radar's aspect angle. For this research, metallic cylindrical pipes were chosen as targets because they behave most like isotropic point scatterers. That is, their RCS is the same from any azimuth aspect angle

and therefore cylindrical pipes look the same to a radar no matter its position relative to the cylinder.

In the experiments, the cylinder was in an upright position placed on a small box to raise it relative to the transmitting antenna. The approximate RCS of a cylinder, σ_{cyl} is given by [15]

$$\sigma_{cyl} \approx \frac{2\pi r l^2}{\lambda_c} \quad (3.1)$$

where r is the radius, l is the length of the cylinder, and λ_c is the center frequency of the transmitted signal. The target used had the following parameters: $r = 0.0889$ m, $l = 1.524$ m, and $\lambda_c = 0.5217$ m. The orientation of the cylinder can be seen in Figure 3.1. The setup and configurations will be discussed with more detail in Section 3.2.

All data collections were taken in a mostly empty lab room of size 7.45×7.65 m. Figure 3.1 shows a picture of room as seen from the entrance. The lab room is a



Figure 3.1: Lab space where all radar data was collected.

plain space at AFIT that ,although mostly empty, contains various significant reflectors and is subject to radio frequency interference (RFI) from the environment. Figure 3.2 shows a diagram of the room along with significant reflectors in the room. With reference to Figure 3.2 there is a metallic bookshelf in the lower right corner and desks along the left and right wall. The LabVolt radar table and desk sit just to the left of the shelves, and

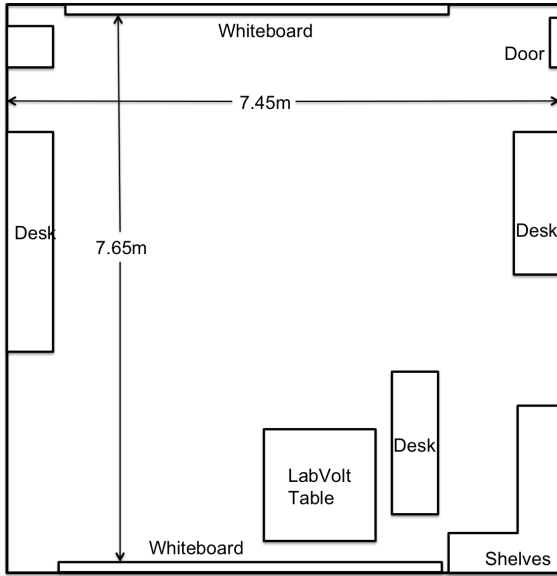


Figure 3.2: Diagram of the room for visual aid

large whiteboards are hung on walls at the top and bottom of the figure. The effect of the clutter in the room will be discussed in more detail in Chapter 4 with the results from each configuration. In addition to the clutter, the room is not isolated from outside sources of RFI, such as that from local radio and tv stations. The clutter and RFI make the detection of targets more difficult than if the room were completely empty. This problem is helped in a number of ways.

One way is to operate the NoNet in the background subtract acquisition mode. Background subtraction works by taking radar data from the scene without the target or targets present and subtracting it from the scene with the target or targets present. Background subtract eliminates stationary scene clutter from the final collected data. The background is specific to a radar's position and viewing angle relative to the scene. For this reason, a background must be taken at each position in the configuration.

Another way is by increasing the SNR via long data length. As explained in Chapter 2, the noise receiver uses correlation to process the received signal. When performing a cross

correlation on noise, the data length affects the SNR. The receiver performs a correlation of the sampled received signal and the sampled transmitted signal. It is shown in [18] that the maximum SNR for the AFIT NoNet is realized when the maximum sampling is used.

The SNR is given by [18]

$$\begin{aligned} SNR &= \rho \sqrt{\frac{K}{\rho^2 + 1}} \\ &\approx \rho \sqrt{K} \quad \text{for } \rho \ll 1. \end{aligned} \tag{3.2}$$

In Equation (3.2) K is the number of samples for each of the transmitted and received waveform and ρ is the cross correlation coefficient. The cross correlation coefficient indicates the strength of correlation between two signals. A maximum correlation of one is achieved when a signal is correlated with an exact copy of itself. The assumption of $\rho \ll 1$ in Equation (3.2) is justified by considering that the received signal from the noise radar is no longer exactly a copy of the transmitted signal after it has propagated through and interacted with the environment.

The SNR can also be increased by averaging multiple collects from the same position. The system does exactly that when configured to record multiple triggers. In the experiment performed the system was configured to record 15 triggers per acquisition. Averaging across the triggers increases the SNR by ensuring stable returns are preserved and anomalous spikes or troughs are averaged out.

The three approaches to increase SNR discussed above were used for all experiments in order to better detect targets. The full set of system parameters are shown in Table 3.1. The relationship between the run time, acquisitions, triggers, and sampling period are illustrated in Figure 3.3.

For this research the all elevation angles of the radar nodes relative to the scene is 0° . Per this arrangement the radar, targets, and collected phase history lie in the same plane. All images are therefore collapsed into the image plane.

Table 3.1: Noise Network Parameters

Parameter	Configuration
Radar Mode	Monostatic
Radar Source	Analog
Tx Filter	Enabled
Rx Filter	Enabled
Tx Attenuation	0 dB
Rx Attenuation	0 dB
Run Time	10 s
Sampling	6000 Ms/sec
Triggers	15 per Acquisition
Acquisition Mode	Background Subtract
Acquisition	$1e^{-6}$ s
Correlation	$1e^{-7}$ s

3.2 Node Configurations

As the AFIT NoNet matures, one of its potential uses is radar imaging from a mobile platform. For example, the NoNet nodes may be mounted on a formation of UAVs and flown over a scene of interest. Just like any other imaging application, a radar user needs to define standards for the image quality a system produces. This research looks specifically at computational complexity and image resolution in both range and cross-range. As seen in Chapter 2 image quality depends on various factors, including spatial distribution, system bandwidth, synthetic aperture extent, and sample spacing. The imaging algorithms discussed have their advantages and disadvantages regarding these factors and tradeoffs in terms of computational complexity, or equivalently, the amount of time it takes to generate

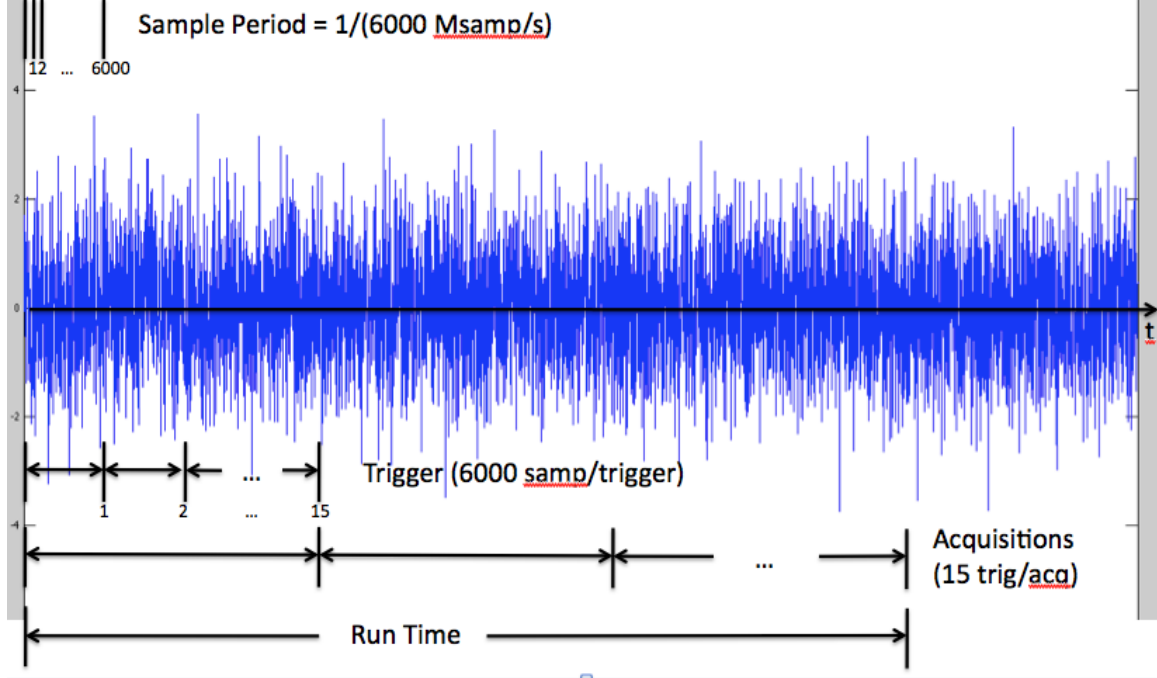


Figure 3.3: Plot illustrating the relationships between the radar's run time, acquisitions, triggers, and sampling period. The sampling frequency is 6000 Msamp/s, each acquisition consists of 15 triggers per acquisition.

an image. The following sections describe the design of the node configurations, their purpose, and each configuration's expected range and cross-range resolutions.

3.2.1 Arc Configuration.

The purpose of the arc layout is to explore image quality from a configuration in which the synthetic aperture is created over a wide angular extent, but with few collects. The configuration was designed to mimic a circular path because it is the simplest case for spotlight SAR. The position of the nodes is such that each has the same range to the scene center and azimuth spacing intervals are equal. Figure 3.4 shows the layout of the arc configuration and Table 3.2 lists the coordinates of the radar nodes and target positions.

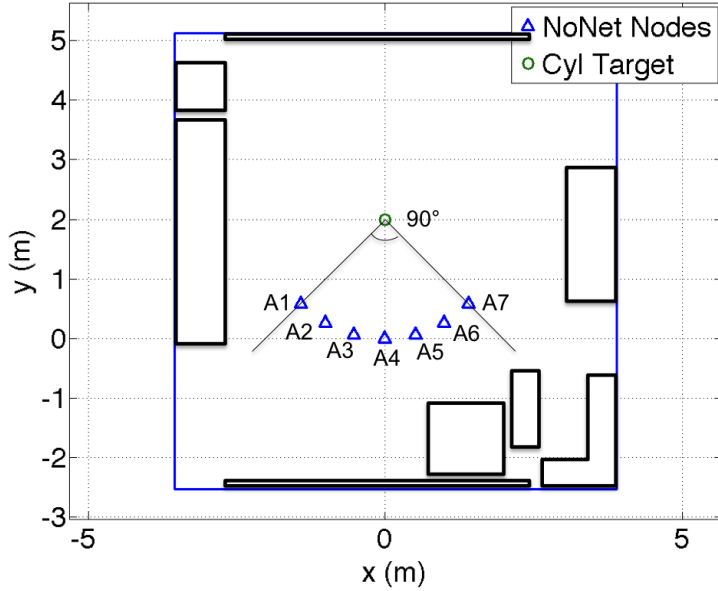


Figure 3.4: Arc Configuration - The relative positions of the walls and significant clutter are indicated in the figure, see also Figure 3.2.

The arc configuration has a large aperture extent of 90° with 15° azimuth spacing. The cylindrical target was placed at $(0, 2)$ m. In this layout, range is along the y -axis and cross-range is along the x -axis. Node A4 is considered the reference node at position $(0, 0)$ m. The azimuth angles are measured relative to the target where 0° is along the negative y -axis and positive angles are measured counter clockwise toward the positive x -axis. The reference node, A4, has an azimuth of 0° .

As shown in Chapter 2 the mono-static range resolution depends on the system's bandwidth and should be the same for the SAR algorithms regardless of the configuration. The AFIT NoNet is bandlimited from around 350 MHz to 800 MHz and has a bandwidth of $B = 450$ MHz. The expected range resolution is (calculated using Equation (2.3)):

$$\rho_r = \frac{c}{2B} = \frac{3 \times 10^8 \text{m/s}}{2(450 \times 10^6 \text{Hz})} = 0.333 \text{m.} \quad (3.3)$$

Table 3.2: Arc Configuration

Node	Node Coordinates	Azimuth
	(x,y) (m)	Angle (deg)
A1	(-1.410, 0.586)	-45
A2	(-1.000, 0.268)	-30
A3	(-0.518, 0.068)	-15
A4	(0.000, 0.000)	0
A5	(0.518, 0.068)	15
A6	(1.000, 0.268)	30
A7	(1.410, 0.586)	45
Target	(0.000, 2.000)	-

Also shown in Chapter 2, the expected cross-range resolution depends on the system's center wavelength and aperture extent. The center wavelength of the system is $\lambda_c = c/f_c$, where c and f_c are the speed of light and the system's center frequency, respectively. The expected cross-range resolution for this configuration is (calculated using Equation (2.10)):

$$\rho_x = \frac{\lambda_c}{2\Delta\phi} = \frac{\frac{3 \times 10^8 \text{m/s}}{575 \times 10^6 \text{Hz}}}{2\left(90 * \frac{\pi}{180}\right) \text{rad}} = 0.166 \text{m}. \quad (3.4)$$

3.2.2 Line Configuration.

The purpose of the line layout is to explore image quality from a configuration similar to the arc configuration, but with a few key differences. Similar to the arc configuration, the synthetic aperture is created over a wide angular extent with few collects. However, the line configuration mimics a straight path rather than an arc. For spotlight SAR in the line configuration, the distance from any point on a straight path to the scene center is different. Also, the node positions for this layout were chosen so that the azimuth spacing intervals

are irregular, that is, they are not evenly spaced. Figure 3.5 shows the layout of the line configuration and Table 3.3 lists the coordinates of the radar nodes and target positions.

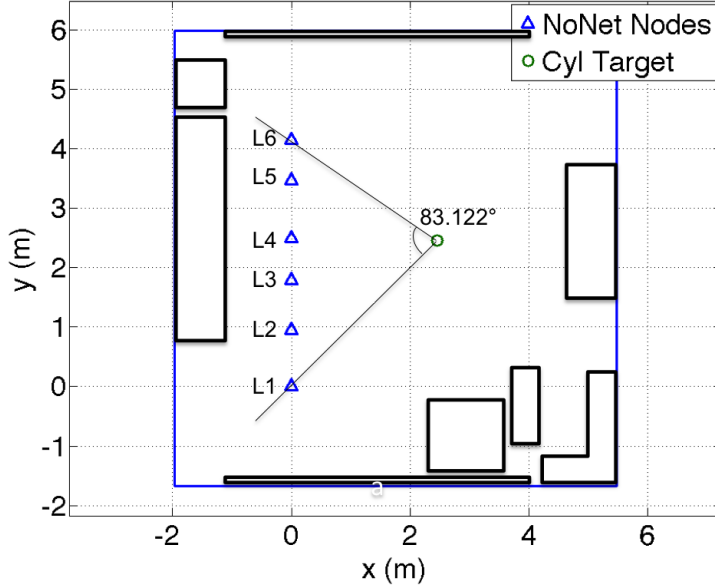


Figure 3.5: Line Configuration - The relative positions of the walls and significant clutter are indicated in the figure, see also Figure 3.2.

The line configuration has a large aperture extent of 83.122° . The azimuth spacing varies randomly from 11.681° to 27.621° . The cylindrical target was placed at $(2.45, 2.45)$ m. The azimuth angles are measured relative to the target where 0° is along the negative y -axis and positive angles are measured counter-clockwise toward the positive x -axis. Node L1 is considered the reference node at position $(0, 0)$ m. The reference node has an azimuth of -44.099° . In this layout, range is along the line bisecting the aperture extent and cross-range is perpendicular to the range. The bisecting line is along the azimuth angle -85.66° .

Table 3.3: Line Configuration

Node	Node Coordinates	Azimuth
	(x,y) (m)	Angle (deg)
L1	(0.000, 0.000)	-44.099
L2	(0.000, 0.950)	-56.675
L3	(0.000, 1.790)	-70.982
L4	(0.000, 2.490)	-98.603
L5	(0.000, 3.470)	-115.540
L6	(0.000, 4.140)	-127.221
Target	(2.450, 2.450)	-

The range resolution, $\rho_x = 0.333$ m, is the same as that of the arc configuration, and is given by Equation (3.3). The cross-range resolution for this configuration, given by Equation (2.10), is

$$\rho_x = \frac{\lambda_c}{2\Delta\phi} = \frac{\frac{3e^8 \text{m/s}}{575e^6 \text{Hz}}}{2\left(83.122 * \frac{\pi}{180}\right) \text{rad}} = 0.180 \text{m.} \quad (3.5)$$

3.2.3 Cluster Configuration.

The purpose of the cluster layout is to explore image quality from a configuration whose synthetic aperture is created over a narrow aperture extent with few collects. The node positions in the cluster were chosen at random to simulate a tight grouping. In this layout, the radar sensors are taking data of the scene from nearly the same point of view. The distance from each position to the scene center varies. Figure 3.6 shows the layout of the cluster configuration and Table 3.4 lists the coordinates of the radar nodes and target positions.

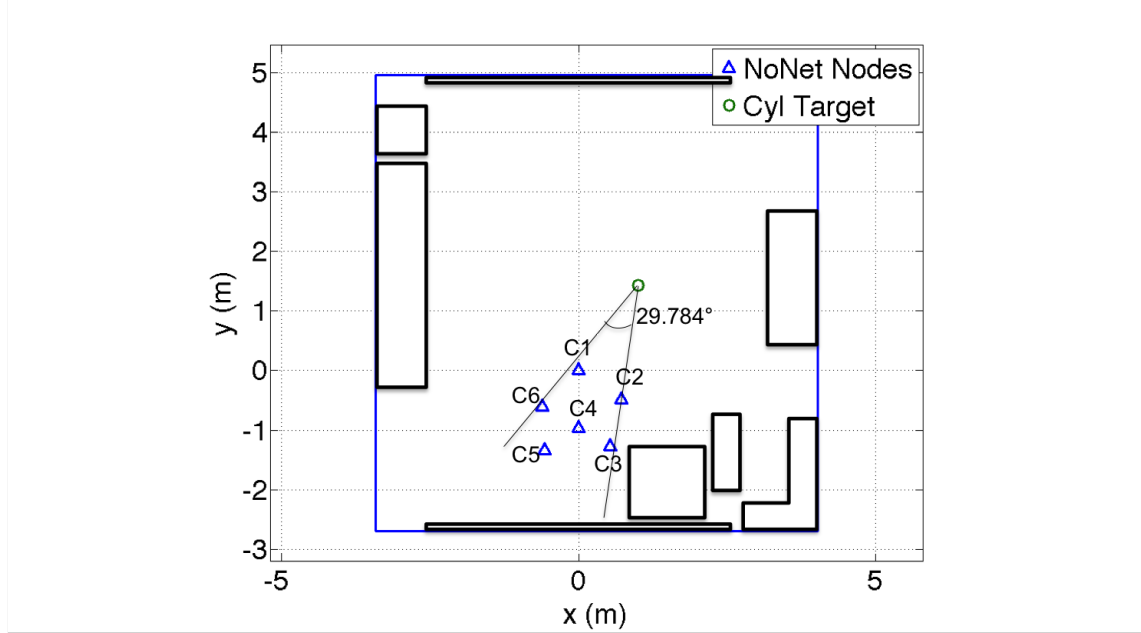


Figure 3.6: Cluster Configuration - The relative positions of the walls and significant clutter are indicated in the figure, see also Figure 3.2.

The cluster configuration has a small aperture extent of 29.784° . The azimuth spacing varies from 1.418° to 12.837° . The cylindrical target was placed at $(1.0, 1.425)$ m. The azimuth angles are measured relative to the target where 0° is along the negative y -axis and positive angles are measured counter-clockwise toward the positive x -axis. Node C1 is considered the reference node at position $(0, 0)$ m. The reference node has an azimuth of -34.611° . In this layout, the range is along the line bisecting the aperture extent and cross-range is perpendicular to the range. The bisecting line is along the azimuth angle -23.097° .

As discussed earlier, the range resolution, $\rho_r = 0.333$ m, is the same as that of the arc configuration, and is given by Equation (3.3). The cross-range resolution for this configuration, given by Equation (2.10), is

$$\rho_x = \frac{\lambda_c}{2\Delta\phi} = \frac{\frac{3 \times 10^8 \text{ m/s}}{575 \times 10^6 \text{ Hz}}}{2 \left(29.784 * \frac{\pi}{180} \right) \text{ rad}} = 0.5018 \text{ m.} \quad (3.6)$$

Table 3.4: Cluster Configuration

Node	Node Coordinates	Azimuth
	(x,y) (m)	Angle (deg)
C1	(0.000, 0.000)	-34.611
C2	(0.721, -0.486)	-8.205
C3	(0.539, -1.270)	-9.623
C4	(0.000, -0.970)	-22.460
C5	(-0.570, -1.344)	-29.341
C6	(-0.601, -0.601)	-37.989
Target	(1.000, 1.425)	-

3.2.4 Surround Configuration.

The purpose of the surround layout is to explore image quality from a configuration whose synthetic aperture is created over a very wide angular extent with few collects. In this case, the scene is observed from all sides and the nodes are spread very far apart. Each position has a unique distance to the scene center and the azimuth spacing between the nodes varies. Figure 3.7 shows the layout of the surround configuration and Table 3.5 lists the coordinates of the radar nodes and target positions.

The surround configuration has a very large aperture extent of 277.683°. The aperture extent was found by subtracting the largest azimuth space between adjacent nodes from a full 360°. The azimuth spacing between the nodes varies from 42.177° to 82.317°. The cylindrical target was placed at (0.0, 2.0) m. In this layout the range is along the y-axis and the cross-range is along the x-axis. Node S1 is considered the reference node at position (0, 0) m. The azimuth angles are measured relative to the target where 0° is along the

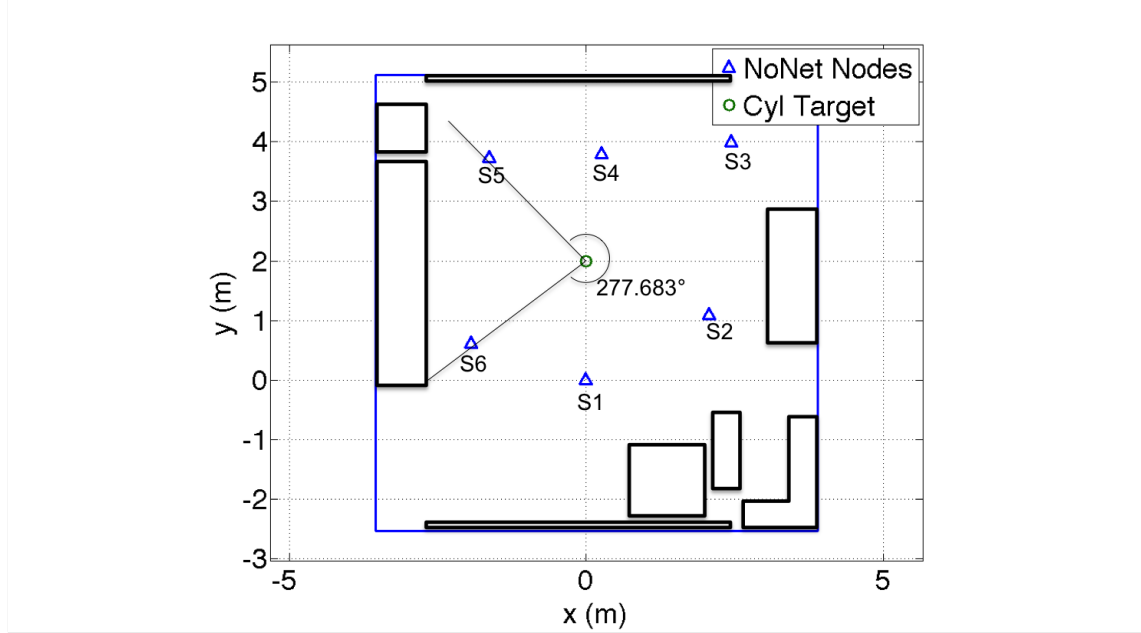


Figure 3.7: Surround Configuration - The relative positions of the walls and significant clutter are indicated in the figure, see also Figure 3.2.

negative y -axis and positive angles are measured counter clockwise toward the positive x -axis. The reference node, S1, has an azimuth of 0° .

Again, the range resolution, $\rho_r = 0.333$ m, is the same as that of the arc configuration, and is given by Equation (3.3). The cross-range resolution for this configuration is given by equation Equation (2.10) is

$$\rho_x = \frac{\lambda_c}{2\Delta\phi} = \frac{\frac{3 \times 10^8 \text{m/s}}{575 \times 10^6 \text{Hz}}}{2 \left(277.683 * \frac{\pi}{180} \right) \text{rad}} = 0.054 \text{m.} \quad (3.7)$$

Note that in this layout, as you move along the synthetic aperture there is a point where the range direction becomes the cross-range direction and vice-versa. Given this, the resolution in both the x and y directions should approach the finer of the range and cross-range resolutions, that is both range and cross-range resolutions should approach ρ_x as computed in Equation (3.7), so the range resolution is modified to $\rho_r = \rho_x = 0.054$ m.

Table 3.5: SurroundConfiguration

Node	Node Coordinates	Azimuth
	(x,y) (m)	Angle (deg)
S1	(0.000, 0.000)	0.000
S2	(2.074, 1.084)	67.090
S3	(2.439, 3.994)	129.751
S4	(0.259, 3.791)	171.928
S5	(−1.629, 3.730)	−137.289
S6	(−1.937, 0.607)	−54.972
Target	(0.000, 2.000)	—

3.3 Image Formation, Resolution Measuring, Computation Timing

Following the collection of data for the configurations described in Section 3.2, three imaging algorithms were used to process the data: Multilateration, Convolution Backprojection, and Polar Format. Sections 3.3.1, 3.3.2, and 3.3.3 describe the algorithms and Section 3.3.4 describes how resolutions were determined from the images formed by the data. Section 3.3.5 outlines how each method was timed for a measure of computational complexity.

3.3.1 *Multilateration Algorithm.*

Multilateration, discussed in Chapter 2, uses multiple nodes and their coordinates along with the timing of the received noise signals to locate a target. The NoNet uses the timing of the received signals to translate the data into a profile of received signal strength intensity which can be matched to a range scale based on sampling rate. The multilateration images were produced with a slightly modified version of code written by Captain John Priestly and Major Matthew Nelms [14].

The multilateration algorithm works as follows:

- Inputs are node coordinates and the received range profiles from each node. In order for this code to work correctly, there must be a reference node at the origin (0, 0) m.
- Define range extent, R_{ext} of the image. The range extent of the image is based on two values: the highest magnitude of either of the x or y coordinate of the nodes, and the distance between the target and the furthest node.
- Define the image. In this thesis three sizes of $N \times N$ images were formed: $N = 256$, 512, and 1024
- Create interpolation grids in x and y . In essence, the 1D range profiles of each node will be swept around in a circle about its coordinates creating a 2D image. The interpolation grids are a meshgrid of x and y vectors, each from $-R_{ext}$ to R_{ext} .
- Create a radius grid and an index grid for each node. The radius grid uses the interpolation grids in the previous step to form a grid of radial distances centered at each nodes coordinates. An index grid corresponding to the radius grid is then created. The index grid is used to map the values of the range profiles and create the intensity matrix (the image)
- Finally, each range profile's intensity is mapped to its respective index grid. The image data is formed by the non-coherent sum from each range profile's contribution to the image.

The code is simple compared to the SAR algorithms. It only uses the profile intensities from each node and adds their contribution to an interpolated 2D grid. Fourier techniques are not used in this method nor are they needed as the NoNet measures range directly through time of flight.

For images formed with this algorithm you should expect to see the reference node at the origin. The target location is determined by the summed contribution of the range intensities from each node. Images were formed using both the raw summed intensities in millivolts and data converted to decibels. The decibel images were normalized and a threshold of -3 dB was applied.

3.3.2 *Backprojection Algorithm.*

Backprojection, discussed in Chapter 2, takes a collection of projections taken from different angles and backprojects the values of the projections onto corresponding x, y coordinates. Each pixel accumulates some value from the projections corresponding to its distance from the scene center and the angle from which the projection was collected. The images created using backprojection were produced with a modified version of a backprojection algorithm written by LeRoy Gorham and Dr. Julie Jackson [4]. Dr. Jackson corrected the code to include a filter in the frequency domain. In the derivation for the backprojection reconstruction equation in Section 2.2.2.2, the reflectivity function a scene, $g(x, y)$ is rewritten in polar coordinates. In Equation (2.16) the Jacobian, $|U|$, resulting from the cartesian to polar coordinate change. As noted, the inner integral in Equation (2.17) is equivalent to a convolution of the projections $g_p(u, \phi)$ with a filter with a frequency response of the inverse Fourier transform of $|U|$. The filter was omitted in Gorham's original code.

The backprojection code works as follows:

- Inputs are system bandwidth, each node's received range profile, azimuth angle, and range to scene center. Each range profile is modified to account for the range to the scene center by shifting the data in the vector.
- The time domain NoNet range data is converted to phase history by performing an FFT and then passed to the backprojection algorithm.

- The backprojection algorithm creates a vector corresponding to the range to each bin in the profile and interpolates the calculated differential ranges to each pixel in the image for each node.
- An IFFT is performed on the phase history for each node to reform the range profile, preserving the phase history.
- Finally, each range profile is mapped to the image grid and the image is formed by the coherent-sum from each range profile's contribution to the image. Since phase history is preserved, the sum at each pixel will have a phase terms that may constructively or destructively add up.

Images formed with this algorithm will look different from those formed by multilateration. In backprojection images, rather than the reference node, the scene center is located at the origin. In each of the configurations discussed in Section 3.2, the single cylindrical target was positioned at the scene center. Images were formed using in both millivolt and decibel scales. The decibel images were normalized and a threshold of -3 dB was applied.

3.3.3 Polar Format Algorithm.

Polar format algorithm, discussed in Chapter 2, forms images by performing a 2D IFFT on phase history data. For spotlight SAR, the data that is collected falls on a polar raster. The polar format algorithm must first interpolate the data onto a Cartesian grid in order to utilize the 2D IFFT. The images created using the polar format algorithm were produced with code written by Brian Rigling and Dr Julie Jackson.

The polar format algorithm works as follows:

- Inputs are system bandwidth, each node's received range profile, azimuth angle, and range to scene center. Each range profile is modified to account for the range to the scene center by shifting the data in the vector.

- The time domain NoNet range data is converted to phase history by performing an FFT.
- The Cartesian coordinates of the polar raster data are calculated and the average x and y values are used to create a Cartesian interpolation grid.
- Interpolation of the data is performed first along the range direction, then along the cross-range direction.
- The image is formed by performing a 2D IFFT.

Images formed with this algorithm will, like the backprojection algorithm, have the scene center at the origin. In each of the configurations discussed in Section 3.2, the single cylindrical target was positioned at the scene center. Images were formed using in both millivolt and decibel scales. The decibel images were normalized and a threshold of -3 dB was applied.

3.3.4 Determination of Resolution.

The criteria for measuring the resolution is a 3 dB roll off from the max target peak, or equivalently, a half power drop off from the max target peak. This is more easily determined by analyzing the image data in decibel form. Each configuration has a unique layout in terms of node positions and azimuth angles which could skew results if the range and cross-range resolutions were simply measured along the x and y axes. In order to ensure that range and cross-range resolutions are equivalent and comparable, the range direction is measured along the center of the synthetic aperture. For example, for a synthetic aperture that ranges from -15° to 15° , the range direction is along 0° , and for an aperture that ranges from -5° to 25° , the range is along 10° . The cross-range resolution is measured perpendicular to the range. Table 3.6 shows a summary of the alias free scene extents and the expected resolutions that were calculated in Section 3.2 for use in data analysis.

Table 3.6: Expected Range and Cross-range Resolutions and Un-aliasing Range and Cross Range Extents for SAR Images

Configuration	Resolution (m)		Un-aliasing Range (m)	
	ρ_r	ρ_x	W_r	W_x
Arc	0.333	0.166	1000	0.7162
Line	0.333	0.180	1000	0.6462
Cluster	0.333	0.502	1000	1.8019
Surround	0.333	0.054	0.1737	0.1737

3.3.5 *Timing For Computational Complexity.*

The measure for computational complexity is timing. The computer used for running the algorithms was a MacBook Pro running OS X 10.9.2 with 2.8 GHz Intel Core 2 Duo Processor and 8 GB of memory. Matlab's tic-toc function was used to time the image forming process of the algorithms. Each algorithm was modified to produce images of three sizes; 256×256 , 512×512 , and 1024×1024 pixels. The final timing result was taken as the average time of 20 runs at each size. The timing for the SAR algorithms will be compared to their expected computational complexities, which are discussed in Sections 2.2.2.1 and 2.2.2.2.

3.4 Chapter Summary

This chapter discussed the research methodology and described the procedures used to perform experiments. The purpose of the research is to compare SAR images formed using various signal processing methods for radar systems set up in various configurations. Images will be compared according to metrics of image resolution, contrast ratio, and computational complexity. These results can be used to evaluate trade-offs between errors and computational cost. For example, in a situation where the processed images are needed

near real time, it would not make sense to choose the signal processing method that takes hours to generate images. On the other hand, a faster algorithm might not provide the resolution required to detect and resolve targets depending on the shape of the synthetic aperture. This research aims to identify the trade-offs in order to find what combination of radar system configuration and signal processing method fits best with required scenarios.

IV. Results

In Chapter 4 the images created with the imaging algorithms discussed in Chapter 2 and Chapter 3 are analyzed and compared to expected results and to each other.

4.1 Image Results of the Arc Configuration

The arc configuration simulates data being taken from a platform traveling on a circular path around the scene of interest. In this thesis, it is the easiest case to deal with because the range from each node to the scene center is the same distance and the nodes are regularly spaced over the synthetic aperture.

4.1.1 *Arc Image Results Using Multilateration.*

Figure 4.1 and Figure 4.2 show images resulting from processing the collected data using the multilateration algorithm. The figures include boxes showing the node positions, similar to that in Figure 3.4.

One can see from the images that the multilateration imaging technique works well for the arc configuration. In this configuration the AFIT NoNet provided decent resolution. For multilateration, there is no expected resolution, as the configuration and spatial distribution influence the actual resolution. However, it was stated in Chapter 2 that the finest possible resolution of a multilateration system in both range and cross-range is determined by the monostatic range resolution of a single node. The monostatic range resolution of the NoNet was calculated in Equation (2.3) as 0.333 m. For the multilateration image generated, the measured resolution in range (along the y -axis) was measured at $\rho_r = 0.5476$ m and the cross-range resolution was measured at $\rho_x = 1.0743$ m.

Although it is obvious to an observer that there is a clear target somewhere around the coordinates (0, 2) m, the images contain artifacts that can be misinterpreted as additional targets. The target is more apparent when the scale is converted to decibels and a -3 dB

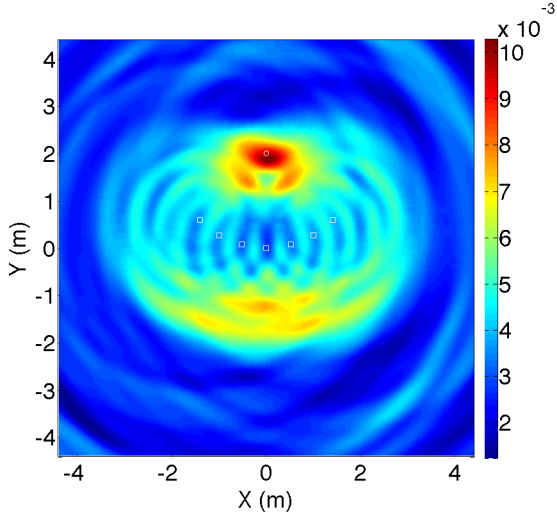


Figure 4.1: Arc configuration multilateration image. The node locations are indicated by white squares and the actual target location is indicated by a white circle.

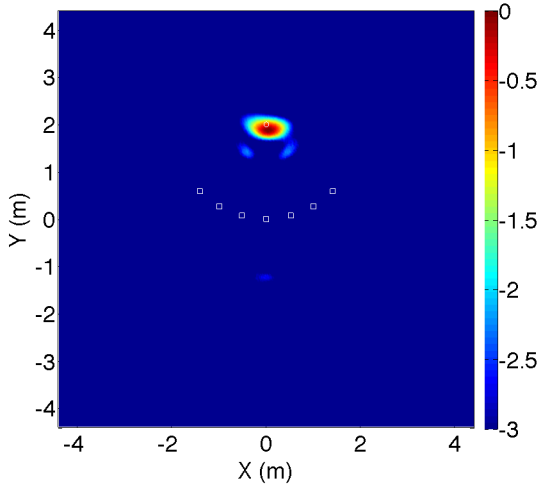


Figure 4.2: Arc configuration multilateration image in dB with -3 dB threshold. The node locations are indicated by white squares and the actual target location is indicated by a white circle.

threshold, consistent with the halfpower resolution rule, is applied. Even with the threshold applied a faint ghost appears around $(0, -1.3)$ m and two faint ghosts appear near the actual target. The ghosts may be explained by examining the range profiles shown in Figure 4.3.

In each, the actual target is the maximum peak. In the range profiles there is another small peak just closer in range. The linear combination of the range contours sum enough to keep the power of that above the half power of the target peak. In this configuration, the linear combination of each node's contribution to the overall image does not raise the target's power enough to remove the doubt of additional targets.

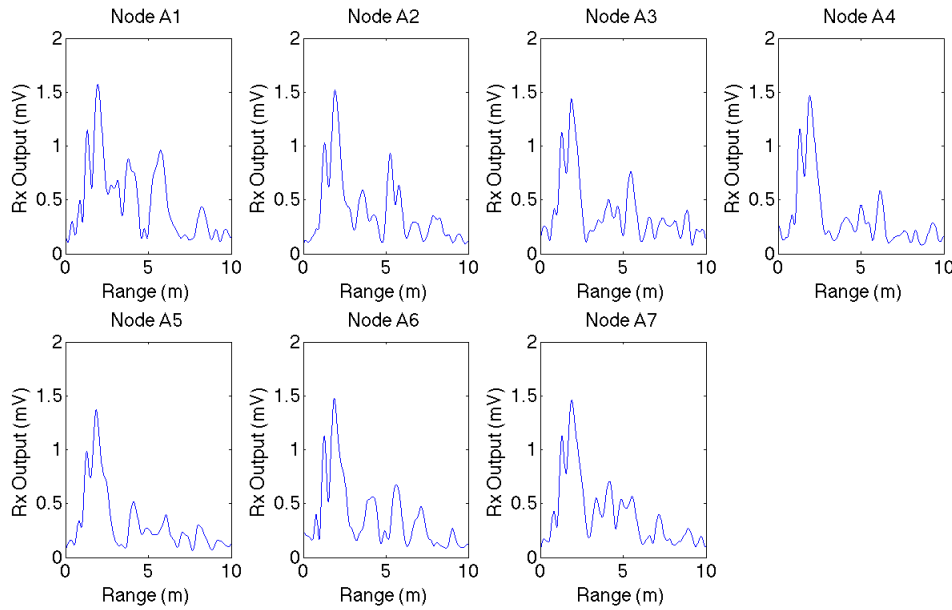


Figure 4.3: Range profiles collected by the nodes in the arc configuration. See also Figure 3.4.

As discussed in Chapter 3, the NoNet system was used to collect data using background subtraction. In a scene with a single point scatterer-like target one would expect a range profile with a single spike corresponding to the range to the target. Figure 4.3 shows the range profiles for the arc configuration out to 10 m collected by the nodes (excludes the reference node with an azimuth angle of 0°). Though background subtraction was used, each node seems to detect smaller returns at ranges beyond the target.

As discussed earlier, the cylindrical target was chosen because it behaves closest to an isotropic point scatterer. As the radar waves interact with the cylinder, some of it is reflected back to the receiver as expected. These reflections result in spikes corresponding to the target range. A cylindrical target also creates forward scattering waves which may then reflect off of other surfaces and be detected by the radar receiver [17]. Unfortunately, background subtraction will not account for the forward scatter which, depending on the scene, can result in false detection of targets. In the arc configuration, the reference node, A_4 , as seen in Figure 3.4, was 5.12 m away from the lab wall behind the target. Nodes A_3 and A_5 are 15° off of the reference node and, with some geometry calculations, you find their direct line distance to the back wall through the target is 5.23 m. Similarly, the distance for nodes A_2 and A_6 are 5.60 m and for A_1 and A_7 are 6.41 m.

For possible forward scatter, the outer nodes, A_1, A_2, A_6 , and A_7 would be expected to detect targets further in range because of two things: they are the furthest from any scatterer (the wall) that is behind the target and they point towards a corner. It is possible that the radar signal can take multiple bounces, thereby increasing the range reading the receiver will detect. The inner nodes, A_3, A_4 , and A_5 have less of an incidence angle with respect to the wall, so one would expect the returns to be near their straight line distances to the wall.

However, given the non-ideal collections discussed, in this case false returns at ranges from about 5 to 6 m do not contribute to the ghosts. The ghost at approximately $(0, -1.3)$ m in Figure 4.2 is caused by returns from the actual target. There is just enough overlap from the range contours of the nodes that the summation around that point exceeds the threshold. Though the returns from scatterers beyond the target do not contribute to target ghosts in this case, the phenomenon will help explain results for other configurations.

Computational expense was also measured by computing the time it takes for the algorithm to form an image from the data. Over 20 instances of image formation,

the average computational time for the multilateration algorithm was recorded and is summarized in Table 4.1. Comparisons to other algorithms will be discussed in Section 4.5.

Table 4.1: Computational complexity for the Arc configuration using Multilateration (Execution time is the average of 20 imaging instances).

Image size <i>N × N pixels</i>	Execution time (s)	Ratio μs/pixel
256×256	0.0066	0.1007
512×512	0.0416	0.1587
1024×1024	0.2041	0.1946
2048×2048	0.8204	0.1996

4.1.2 Arc Image Results Using Convolution Backprojection.

The convolution backprojection images are presented in Figure 4.4 and Figure 4.5. As noted in Chapter 3, in the SAR images the reference node is no longer at the origin and the scene is translated so that the scene center is at the origin. In each scenario the location of the target is the scene center, so one would expect the target to appear at the origin. The translated coordinates of the radar nodes have been plotted for easier comparison to multilateration images.

The measured resolutions of the convolution backprojection generated images are finer in both range and cross-range than that seen for the multilateration images. The measured range and cross-range resolutions and the percent error from theoretical expectations are shown in Table 4.2.

Results for the range resolution somewhat agree with expected values, however the cross-range resolution has an error of over 88% The discrepancies is due to the fact that

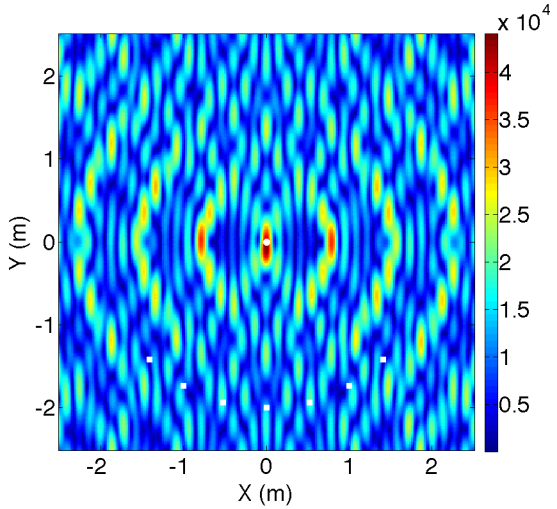


Figure 4.4: Arc configuration backprojection image. The node and target locations are indicated by white squares and a white circle, respectively.

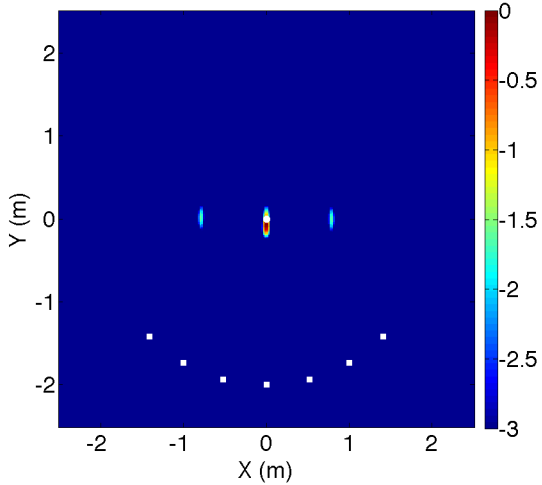


Figure 4.5: Arc configuration convolution backprojection image in dB with -3 dB threshold. The node and target locations are indicated by white squares and a white circle, respectively.

the equations for SAR resolution are for the first null, not the 3 dB distance. The 3dB distance was kept as the measure to stay consistent with the resolution determination for multilateration.

Table 4.2: Resolution results for the backprojection algorithm performed on the arc configuration.

Resolution/un-aliased range (m)	Expected	Measured	% Error
ρ_r	0.3333	0.3914	14.844
ρ_x	0.1660	0.0881	88.422
W_r	1000	—	—
W_x	0.7162	0.7877	9.0770

In the backprojection images there appears to be two target ghosts on either side of the target. However, they are not ghosts, but aliased copies of the target. Aliased copies are the result of under sampling in the spatial frequency domain. Recall from Section 2.2.2 that the alias free range and cross-range extents are given by Equation (2.11) and Equation (2.12), respectively. Fortunately for an UWB signal, like that used by the AFIT NoNet, the alias free range extent, W_r , is not much of an issue. Though it is inversely proportional to the frequency step size, even very coarse sampling will yield a large W_r . For example, the extent of Figure 4.4 in the range direction is 5 m, which requires only 15 frequency samples over the bandwidth of 450 MHz. The image was created with over 3000 frequency samples and the expected $W_r = 1000$ m. The measurement for the un-aliased range extent is beyond the extent of the image and is not actually measured.

The alias free cross-range extent, W_x is inversely proportional to the azimuth step size. In the arc configuration the nodes are evenly spaced by a course 15° . From Equation (2.12) we find that the alias free cross-range extent for this configuration is $W_x = 0.7162$ m. The results for the un-aliased cross-range extent agrees. The measured value had a 9.0770% error from the expected value. This is a problem because targets that are more than W_x m from the scene center will be masked by aliasing.

The computational expense for the backprojection code is summarized in Table 4.3. Comparisons to other algorithms will be discussed in Section 4.5.

Table 4.3: Computational complexity for the Arc configuration using Backprojection (Execution time is the average of 20 imaging instances).

Image size $N \times N$ pixels	Execution time (s)	Ratio $\mu\text{s/pixel}$
256×256	0.1809	2.7603
512×512	0.7712	2.9419
1024×1024	3.3980	3.2406
2048×2048	13.5135	3.2219

4.1.3 Arc Image Results Using Polar Format Algorithm.

Figure 4.6 and Figure 4.7 show images formed using polar format. The resolutions measured for polar format would benefit from re-measuring in future research. Implementation issues caused differences in the pixel sizes that make comparisons improper.

The computational complexity was measured by computing the time it takes for the algorithm to form the images. The computational time of 20 instances of image formation were averaged and recorded. As discussed in Section 2.2.2.1 the the polar format has $P(N) + N^2 \log N$ complexity, where $P(N)$ is the cost of the interpolation from polar to Cartesian. Since interpolation can be computationally expensive, the computation time of both the interpolation and the 2D IFFT (forming the image) were also recorded. The results are shown in Table 4.4. Comparisons to other algorithms will be discussed in Section 4.5.

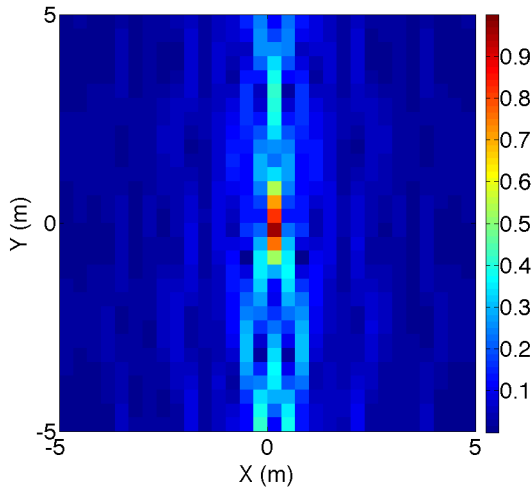


Figure 4.6: Arc configuration polar format image.

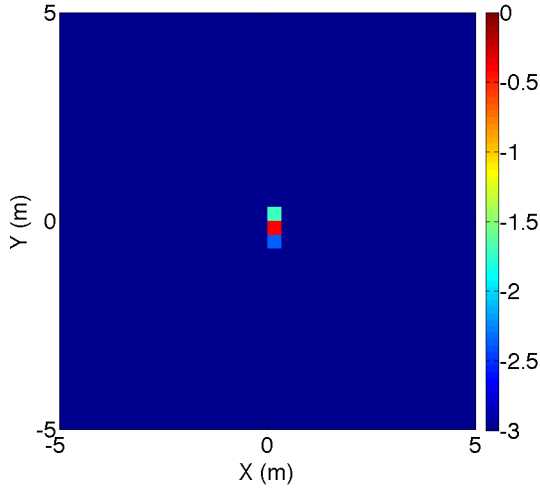


Figure 4.7: Arc configuration polar format image in dB with -3 dB threshold.

4.2 Image Results of the Line Configuration

This section discusses the imaging results of the Line configuration. The node layout simulates data being taken from a platform on a straight path moving by the scene of interest.

Table 4.4: Computational complexity for the Arc configuration using Polar Format Algorithm.

Data Set	Times	Execution Time (s)		
		256 × 256	512 × 512	1024 × 1024
Arc	Interpolation	0.1876	0.3999	0.8752
	Image Formation	0.0075	0.0296	0.1755
	Total	0.1951	0.4295	1.0507

4.2.1 Line Image Results Using Multilateration.

Figure 4.8 and Figure 4.9 display the images for the line configuration created using multilateration. This configuration is much like the arc configuration; however, because of the straight path, the combination of the contour rings indicate targets on both sides of the nodes. Given the directionality of the radar antennas, an analyst would be able to eliminate the false target. As shown in Figure 3.5 the actual target is at the coordinates (2.45, 2.45) m. Like was the case for the arc, the radar nodes picked up targets approximately 5 to 6 m in range as a result of the forward scatter off of the cylindrical target. The configuration and spatial distribution of this case was such that the range contours summed in a way that the false return has enough power to appear as a target.

As discussed in Section 3.2.2 the range direction is measured along -85.66° , the angle bisecting the synthetic aperture extent. To make measurements easier and more accurate, instead of measuring the resolutions along the angles, the scene was rotated so that, like the arc configuration, the range was along the y -axis and the cross-range along the x -axis. The rotated image is shown in Figure 4.10. The measured range and cross-range resolutions were $\rho_r = 0.5496$ m and $\rho_x = 1.1242$ m, respectively.

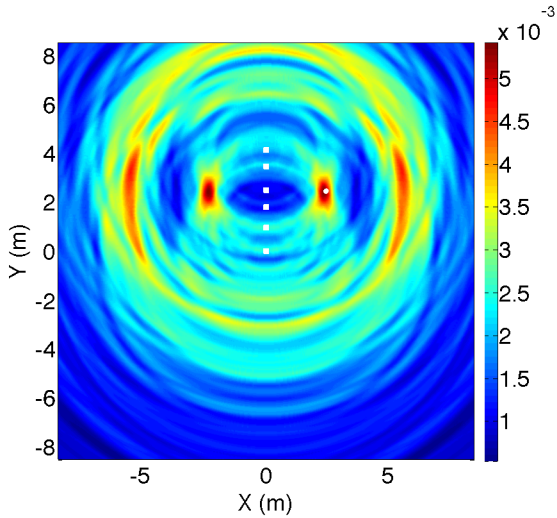


Figure 4.8: Line configuration multilateration image. The node and target locations are indicated by white squares and a white circle, respectively.

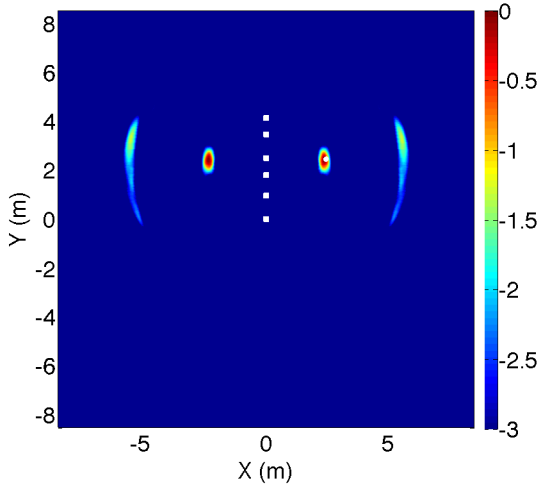


Figure 4.9: Line configuration multilateration image in dB with -3 dB threshold. The node and target locations are indicated by white squares and a white circle, respectively.

The computational expense for the line configuration multilateration imaging is summarized in Table 4.5. Comparisons to other algorithms will be discussed in Section 4.5.

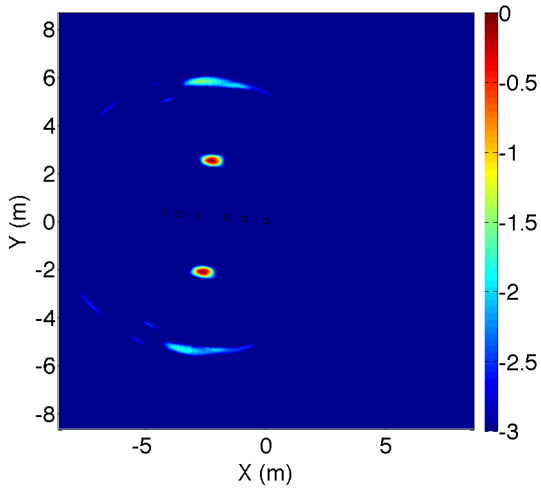


Figure 4.10: Line configuration image rotated so that range and cross-range are in the y and x directions, respectively.

Table 4.5: Computational complexity for the Line configuration using Multilateration
(Execution time is the average of 20 imaging instances)

Image size	Execution	Ratio
$N \times N$ pixels	time (s)	$\mu\text{s/pixel}$
256×256	0.0056	0.0854
512×512	0.0305	0.1163
1024×1024	0.1792	0.1709

4.2.2 *Line Image Results Using Convolution Backprojection.*

Figure 4.11 and Figure 4.12 show the image results when convolution backprojection was used to create images for the line configuration. The location of the nodes is plotted with relation to the target at the scene center.

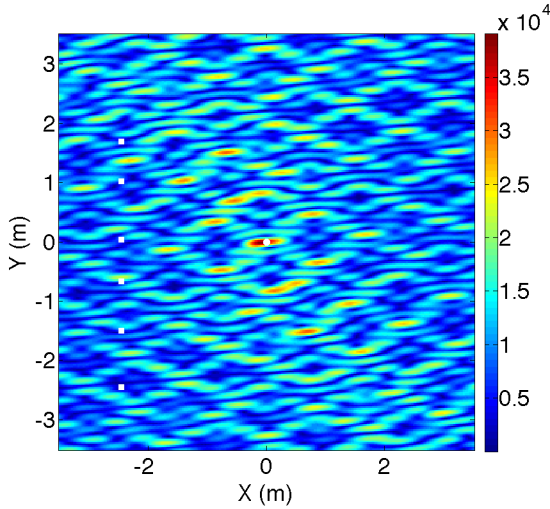


Figure 4.11: Line configuration backprojection image. The node and target locations are indicated by white squares and a white circle, respectively.

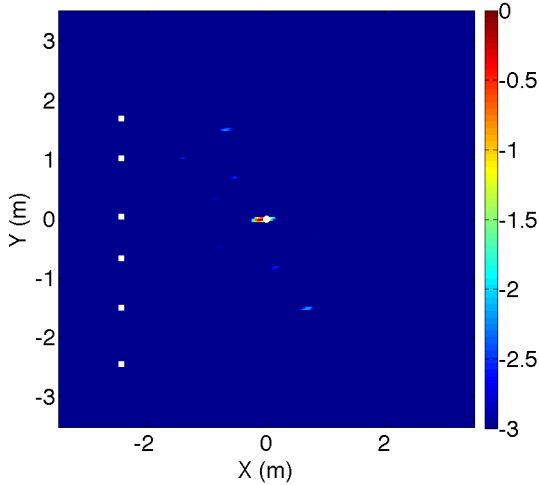


Figure 4.12: Line configuration backprojection image in dB with -3 dB threshold. The node and target locations are indicated by white squares and a white circle, respectively.

The measured resolutions of the convolution backprojection generated images are $\rho_r = 0.4510$ m and $\rho_x = 0.0784$ m, calculated by analyzing a rotated axes. The axes were rotated such that range is measured along the y -axis and cross-range along the x -axis

as shown in Figure 4.13. The measured range and cross-range resolutions and the percent error from theoretical expectations are shown in Table 4.6.

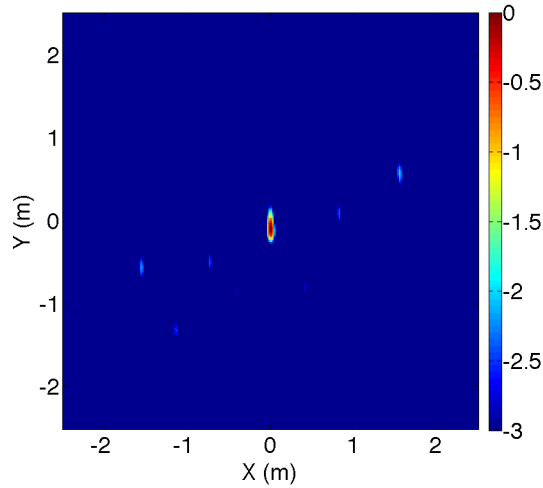


Figure 4.13: Line configuration image rotated so that range and cross-range are in the y and x directions, respectively.

Table 4.6: Resolution results for the backprojection algorithm performed on the line configuration.

Resolution/un-aliased range (m)	Expected	Measured	% Error
ρ_r	0.3333	0.4510	26.098
ρ_x	0.1800	0.0784	129.592
W_r	1000	—	—
W_x	0.6462	0.8098	20.203

The results for resolution do not seem to agree with errors of 26.098% and 129.592%. This discrepancy is due to the fact that the equations for SAR resolution for the first null,

not the 3 dB distance. The 3 dB distance was kept as the measure to stay consistent with the resolution determination for multilateration.

The backprojected image suffers from aliasing in the cross-range direction due to insufficient azimuth sampling. For the line configuration, the alias free cross-range extent is calculated using the mean azimuth spacing of $\delta\phi = 16.6244^\circ$. The measured un-aliased range and cross-range scene extents and the percent error from theoretical expectations are shown in Table 4.6. The un-aliased range is not measured because its is far beyond the extent of the image. The un-aliased cross-range has a 20.203% error from the theoretical expectation.

The computational expense for the backprojection image formation algorithm using the Line configuration is summarized in Table 4.7. Comparisons to other algorithms will be discussed in Section 4.5.

Table 4.7: Computational complexity for the Line configuration using Convolution Backprojection (Execution time is the average of 20 imaging instances).

Image size	Execution	Ratio
$N \times N$ pixels	time (s)	$\mu\text{s/pixel}$
256×256	0.1514	2.3102
512×512	0.6489	2.4754
1024×1024	2.8539	2.7217

4.2.3 *Line Image Results Using Polar Format Algorithm.*

Figure 4.14 and Figure 4.15 show images formed using polar format. The resolutions measured for polar format would benefit from re-measuring in future research.

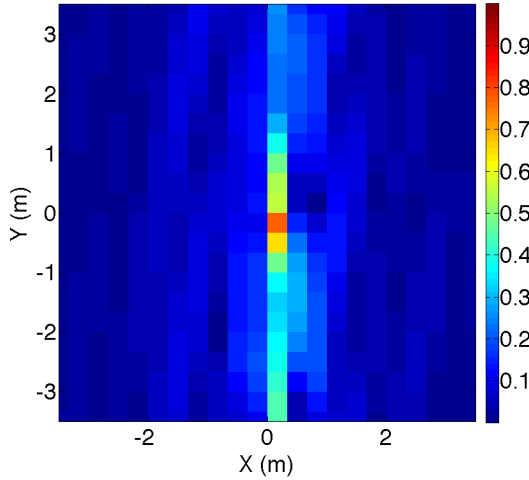


Figure 4.14: Line configuration polar format image.

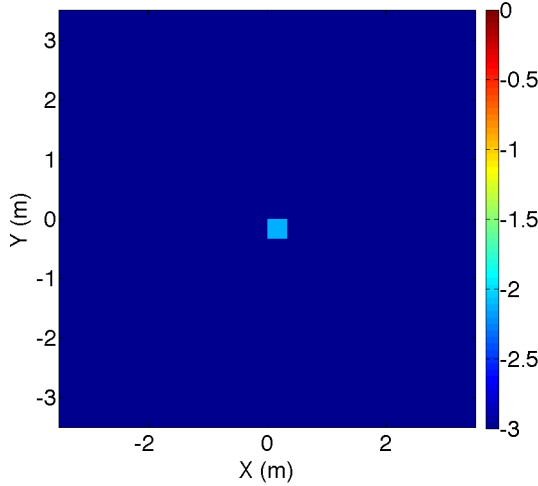


Figure 4.15: Line configuration polar format image in dB with -3 dB threshold.

Implementation issues caused differences in the pixel sizes that make comparisons improper.

The computational complexity was measured by computing the time it takes for the algorithm to form the images. The computational time of 20 instances of image formation were averaged and recorded. Since interpolation can be computationally expensive, the

computation time of both the interpolation and the 2D IFFT (forming the image) were also recorded. The results are shown in Table 4.8. Comparisons to other algorithms will be discussed in Section 4.5.

Table 4.8: Computational complexity for the Line configuration using Polar Format Algorithm.

Data Set	Times	Execution Time (s)		
		256×256	512×512	1024×1024
Line	Interpolation	0.1928	0.4062	0.9064
	Image Formation	0.0076	0.0292	0.1756
	Total	0.2004	0.4355	1.0820

4.3 Image Results of the Cluster Configuration

This section examines the imaging results of the Cluster configuration. This layout is not expected to produce the best results, but is compact and is a viable configuration for real world use.

4.3.1 *Cluster Image Results Using Multilateration.*

Figure 4.16 and Figure 4.17 present the images created using multilateration on the cluster configuration. In this configuration, image quality suffers due to the nodes' close proximity to each other. The finest possible resolution, when using a multilateration imaging technique, occurs at the intersection of two range contours whose nodes are spatially orthogonal with respect to a resolution cell containing the target of interest [14]. The worst resolution occurs when two nodes record a measurement from the same location. In this case their entire range contours will completely overlap and it is impossible to

discern a target. The cluster nodes do not record measurements from the same location, but nearly the same location resulting in the large smearing displayed in the images.

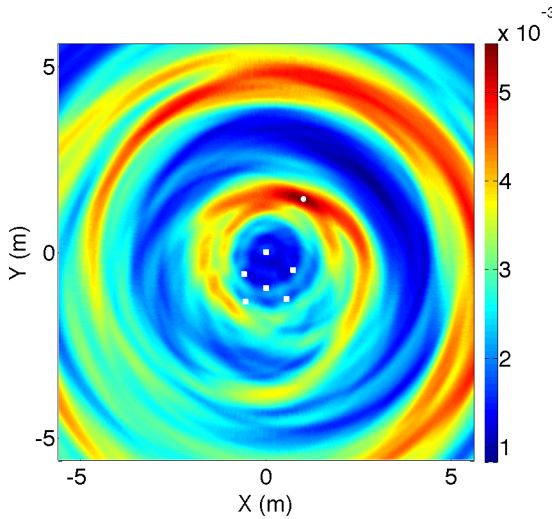


Figure 4.16: Cluster configuration multilateration image. The node and target locations are indicated by white squares and a white circle, respectively.

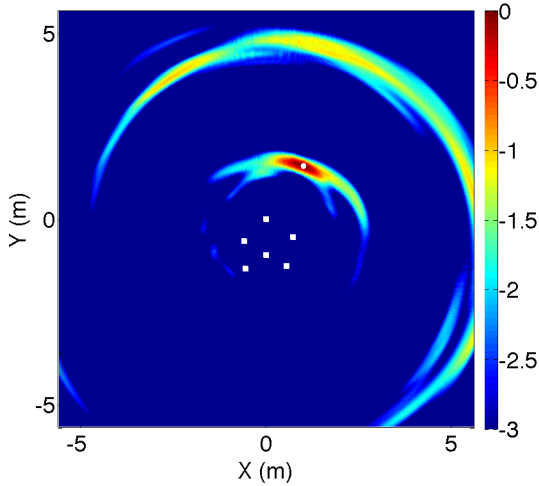


Figure 4.17: Cluster configuration multilateration image in dB with -3 dB threshold. The node and target locations are indicated by white squares and a white circle, respectively.

It was explained in Section 3.2.3 that the range is measured along the angle bisecting the synthetic aperture. For the cluster configuration range is along the line forming a -23.097° through the scene center. For ease of analysis the axes were rotated so that range fell along the y -axis and cross-range along the x -axis, shown in Figure 4.18. As seen in the arc and line configurations, the forward scattering caused false returns to show up behind the target. The smearing from the overlap is emphasized in this configuration since node locations were so near together. The measured range and cross-range resolutions were $\rho_r = 0.5496$ m and $\rho_x = 2.6232$ m, respectively.

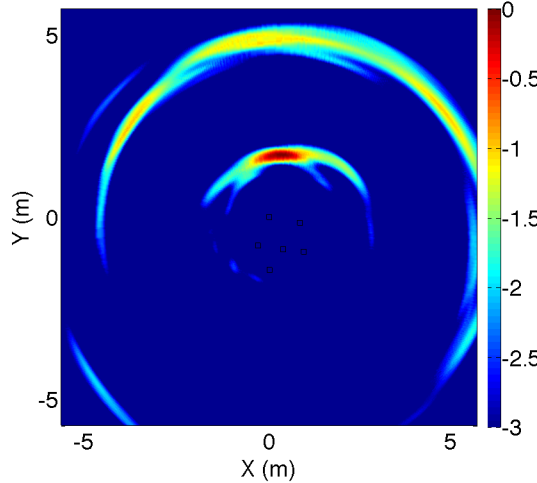


Figure 4.18: Cluster configuration image rotated so that range and cross-range are in the y and x directions, respectively.

The computational expense for the cluster configuration multilateral imaging is summarized in Table 4.9. Comparisons to other algorithms will be discussed in Section 4.5.

Table 4.9: Computational complexity for the Cluster configuration using Multilateration (Execution time is the average of 20 imaging instances).

Image size $N \times N$ pixels	Execution time (s)	Ratio $\mu\text{s/pixel}$
256×256	0.0066	0.1007
512×512	0.0311	0.1186
1024×1024	0.1711	0.1632

4.3.2 Cluster Image Results Using Convolution Backprojection.

Figure 4.19 and Figure 4.20 display the convolution backprojection images from the cluster configuration. The location of the nodes is plotted with relation to the target at the scene center.

Resolutions were analyzed by rotating the image such that range is along the y -axis and cross-range along the x -axis as shown in Figure 4.21. In the cluster configuration, the azimuth extent is small and the cross-range resolution is adversely affected compared to that of the wider aperture configurations. The measured range and cross-range resolutions and the percent error from theoretical expectations are shown in Table 4.10.

Again, the results for resolutions do not seem to agree with errors of 54.520% and 63.439%, due to the fact that the equations for SAR resolutions are for the first null, not the 3 dB distance. The 3 dB distance was kept as the measure to stay consistent with the resolution determination for multilateration.

The un-aliased range extent for the figures easily exceeds the dimension of the image and is around $W_r = 1000$ m. The un-aliased cross-range extent for the cluster configuration improved over the arc and line configurations because the azimuth sampling is finer. The

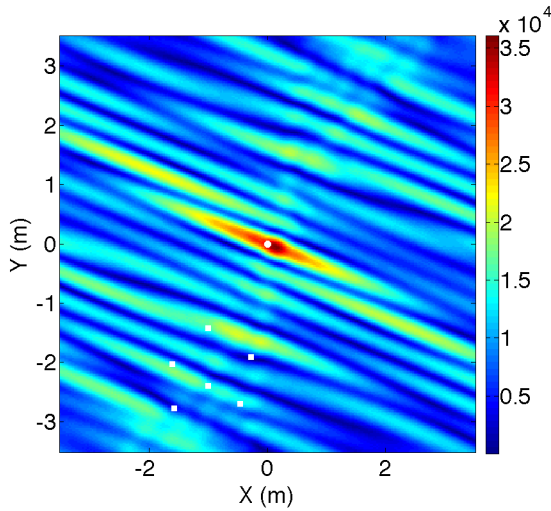


Figure 4.19: Cluster configuration backprojection image. The node and target locations are indicated by white squares and a white circle, respectively.

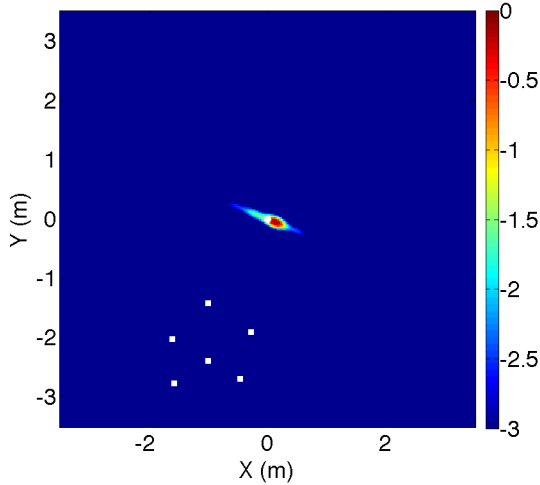


Figure 4.20: Cluster configuration backprojection image in dB with -3 dB threshold. The node and target locations are indicated by white squares and a white circle, respectively.

measured un-aliased range and cross-range extents and the percent error from theoretical expectations are shown in Table 4.10.

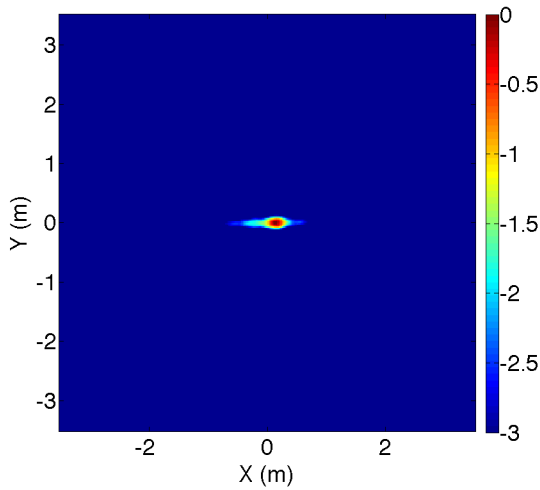


Figure 4.21: Cluster configuration image rotated so that range and cross-range are in the y and x directions, respectively.

Table 4.10: Resolution results for the backprojection algorithm performed on the cluster configuration.

Resolution/Un-aliased range (m)	Expected	Measured	% Error
ρ_r	0.3333	0.2157	54.520
ρ_x	0.5081	1.3725	63.439
W_r	1000	—	—
W_x	1.8019	1.6060	12.198

The result for the un-aliased range is not measured because it is well beyond the image extent. The un-aliased cross-range has an error of 12.198% from the theoretical expectation and somewhat agrees.

The computational expense for the backprojection image formation algorithm using the Cluster configuration is summarized in Table 4.11. Comparisons to other algorithms will be discussed in Section 4.5.

Table 4.11: Computational complexity for the Cluster configuration using Convolution Backprojection (Execution time is the average of 20 imaging instances).

Image size $N \times N$ pixels	Execution time (s)	Ratio $\mu\text{s/pixel}$
256×256	0.1490	2.2736
512×512	0.6363	2.4273
1024×1024	2.8122	2.6819

4.3.3 Cluster Image Results Using Polar Format Algorithm.

Figure 4.22 and Figure 4.23 show images formed using polar format. The resolutions measured for polar format would benefit from re-measuring in future research. Implementation issues caused differences in the pixel sizes that make comparisons improper.

The computational complexity was measured by computing the time it takes for the algorithm to form the images. The computational time of 20 instances of image formation were averaged and recorded. Since interpolation can be computationally expensive, the computation time of both the interpolation and the 2D IFFT (forming the image) were also recorded. The results are shown in Table 4.12. Comparisons to other algorithms will be discussed in Section 4.5.

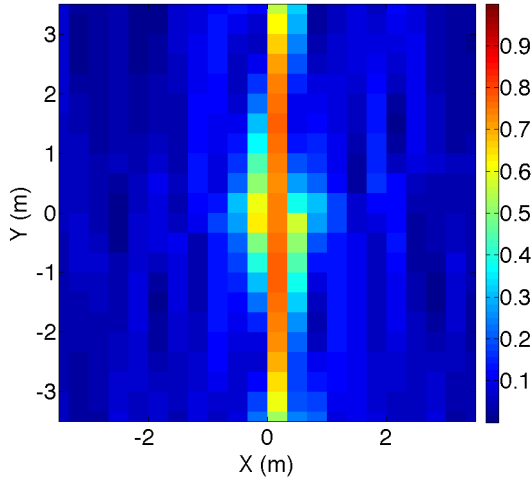


Figure 4.22: Cluster configuration polar format image.

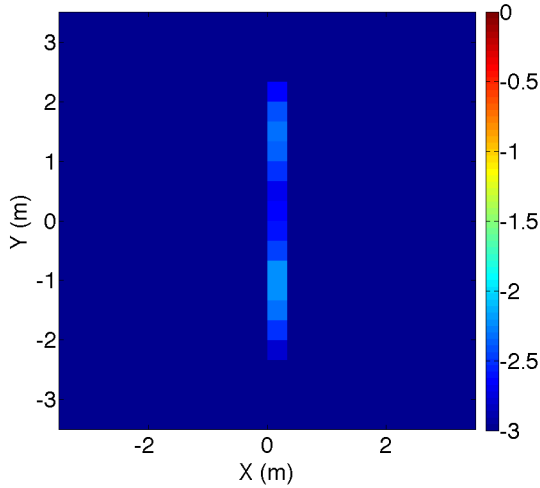


Figure 4.23: Cluster configuration polar format image in dB with -3 dB threshold.

4.4 Image Results of the Surround Configuration

4.4.1 Surround Image Results Using Multilateration.

Figure 4.24 and Figure 4.25 display the images created using multilateration on the surround configuration. The configuration has the widest aperture extent and displays some characteristics of the arc and line configurations. The network detected the target around its actual coordinates of $(0, 2)$ m, however there is a strong ghost target at approximately

Table 4.12: Computational complexity for the Cluster configuration using Polar Format Algorithm.

Data Set	Times	Execution Time (s)		
		256 × 256	512 × 512	1024 × 1024
Cluster	Interpolation	0.1982	0.4131	0.9201
	Image Formation	0.0073	0.0298	0.1744
	Total	0.2054	0.4429	1.0945

(0, 5.6) m. The ghost is the result of the combination of range contours of nodes S3, S4, and S5, which roughly form a line. This phenomenon was seen in Section 4.2.1. Nodes S6, S1, and S2 roughly form an arc. From Figure 4.24 you can see that the nodes forming an arc also sum and form a relatively strong return at approximately (-0.5, -2) m, however not strong enough to exceed the 3 dB threshold. In the surround configuration, the false target spikes resulting from forward scattering can also be seen, however due to the wide distribution of the nodes, the overlap and summation of the range contours keeps the overall intensity much lower than that created by the target.

For this configuration, the range is along the y -axis and cross-range along the x -axis without any adjustments. The measured range resolution of the image is $\rho_r = 0.6496$ m and the measured cross-range resolution is $\rho_x = 1.0743$ m.

The computational expense of the multilateration algorithm on the surround configuration is summarized in Table 4.13. Since the multilateration algorithm operates simply on a collection of range profiles, the execution times are equivalent to the trials performed on the other configurations. Comparisons to other algorithms will be discussed in Section 4.5.

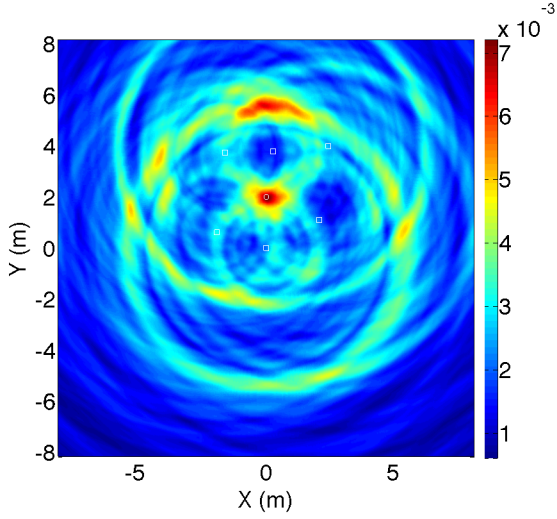


Figure 4.24: Surround configuration multilateration image. The node and target locations are indicated by white squares and a white circle, respectively.

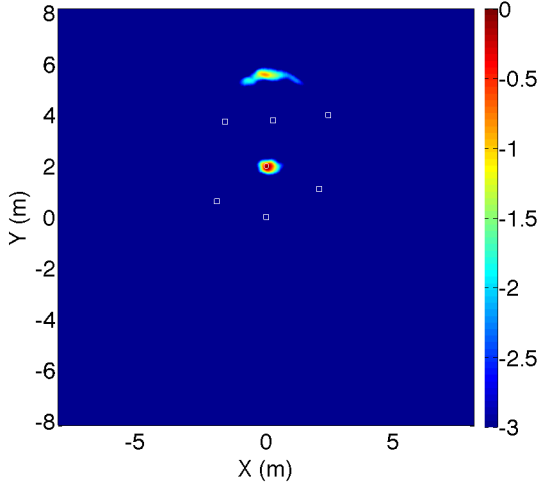


Figure 4.25: Surround configuration multilateration image in dB with -3 dB threshold. The node and target locations are indicated by white squares and a white circle, respectively.

4.4.2 Surround Image Results Using Convolution Backprojection.

Figure 4.26 and Figure 4.27 show the images resulting from performing convolution backprojection on the surround configuration. Since the aperture is so wide, approaching a full 360° , it is reasonable to assume the azimuth or cross-range resolution will overcome

Table 4.13: Computational complexity for the Surround configuration using Multilateration (Execution time is the average of 20 imaging instances).

Image size	Execution	Ratio
$N \times N$ pixels	time (s)	$\mu\text{s/pixel}$
256×256	0.0058	0.0885
512×512	0.0317	0.1029
1024×1024	0.1793	0.1710

the range resolution, resulting in a range resolution that equals the cross-range resolution. However the azimuth sampling is so low that the image suffers greatly from aliasing.

The measured range and cross-range resolutions are equal, $\rho_r = \rho_x = 0.0588$ m. Since the range becomes the cross-range as you move around the node locations, the alias free extent in x and y -axes is equal to the worst case between the two. The poor sampling in azimuth, an average of 61.8434° , drives the alias free range extent of $W_r = W_x = 0.1737$ m. The measured and expected values for resolution and un-aliased range extents are summarized in Table 4.14

Table 4.14: Resolution results for the backprojection algorithm performed on the surround configuration.

Resolution/Un-aliased range (m)	Expected	Measured	% Error
ρ_r	0.0540	0.0588	8.163
ρ_x	0.0540	0.0588	8.163
W_r	0.1737	0.1784	2.634
W_x	0.1737	0.2333	25.547

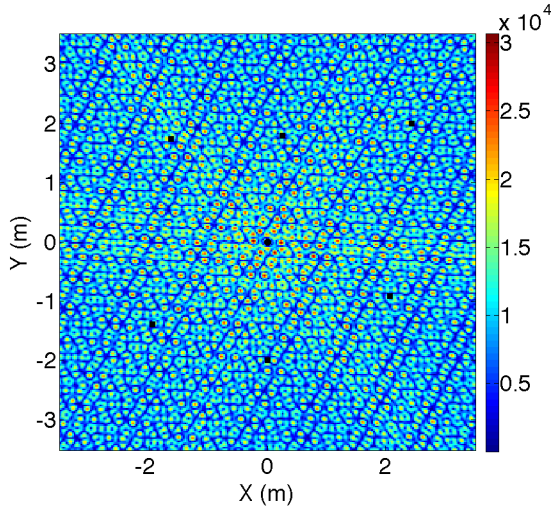


Figure 4.26: Surround configuration backprojection image. The node and target locations are indicated by black squares and a black circle, respectively.

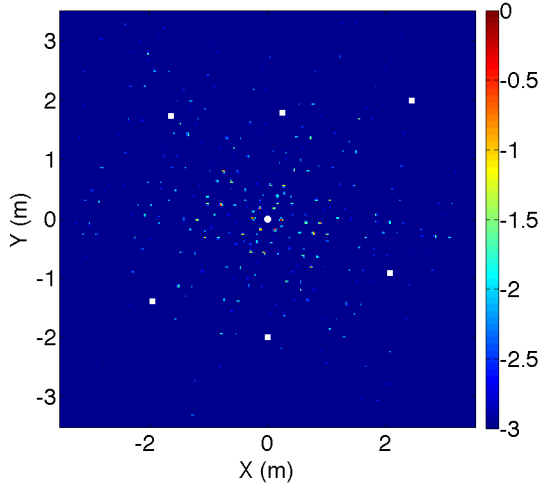


Figure 4.27: Surround configuration backprojection image in dB with -3 dB threshold. The node and target locations are indicated by white squares and a white circle, respectively.

The results for the resolutions in the range and cross-range have an 8.163% error with the expected theoretical results. The results seem to agree. The results for the un-aliased range extents agree in the range direction with a 2.634% error, but the cross-range un-aliased range has a large error and does not agree.

It is difficult to make out the target in Figure 4.26 and Figure 4.27 due to all of the aliased copies. Figure 4.28 shows the scene in a 3D plot. The target can be more easily made out in the center.

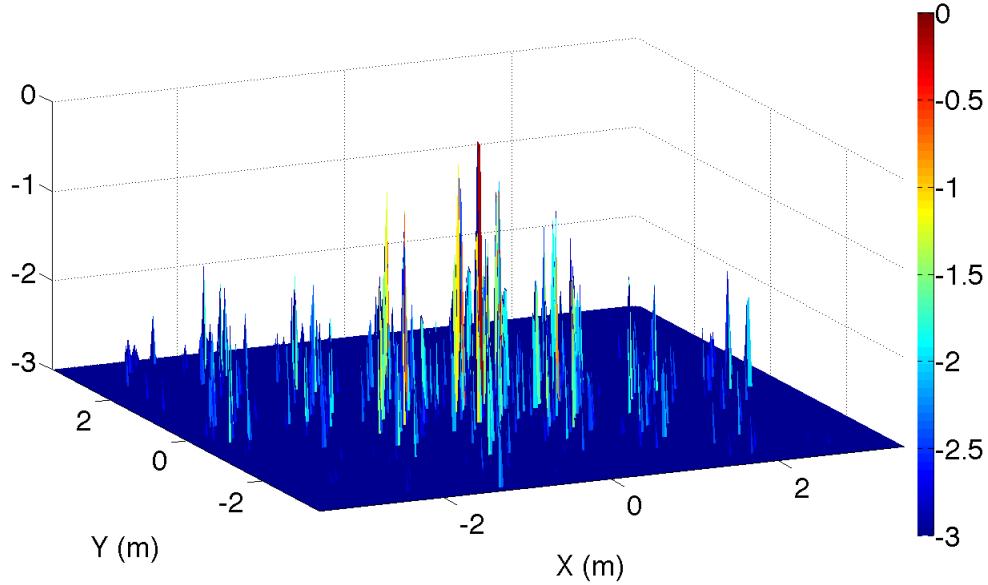


Figure 4.28: Surround configuration image plot in 3D. The target can be made out with very fine resolution due to the nearly 360° azimuth, however poor azimuth sampling results in a poor alias free image diameter.

The computational complexity for using convolution backprojection on the surround configuration is summarized in Table 4.15. Comparisons to other algorithms will be discussed in Section 4.5.

4.4.3 Surround Image Results Using Polar Format Algorithm.

Figure 4.29 and Figure 4.30 show images formed using polar format. The resolutions measured for polar format would benefit from re-measuring in future research.

Table 4.15: Computational complexity for the Surround configuration using Convolution Backprojection (Execution time is the average of 20 imaging instances).

Image size	Execution	Ratio
$N \times N$ pixels	time (s)	$\mu\text{s/pixel}$
256×256	0.1488	2.2705
512×512	0.6385	2.4357
1024×1024	2.8593	2.7268

Implementation issues caused differences in the pixel sizes that make comparisons improper.

The surround images were generated using the same polar format code as other configurations. The fact that there is no response illustrates that the polar format algorithm cannot be used on an arrangement like the surround configuration. Interpolation of a phase history over an aperture as wide as the surround configuration’s aperture is very inaccurate since polar format algorithm should only be used on relatively small angles. In order to successfully apply polar format for this configuration, the algorithm must be modified. An example possibility would be to split the total aperture into smaller subapertures and combine the separately generated images.

The computational complexity was measured by computing the time it takes for the algorithm to form the images. The computational time of 20 instances of image formation were averaged and recorded. The results are shown in Table 4.16.

4.5 Comparison of Results

A summary of the computational execution times and resolutions is shown in Table 4.17 and Table 4.22, respectively.

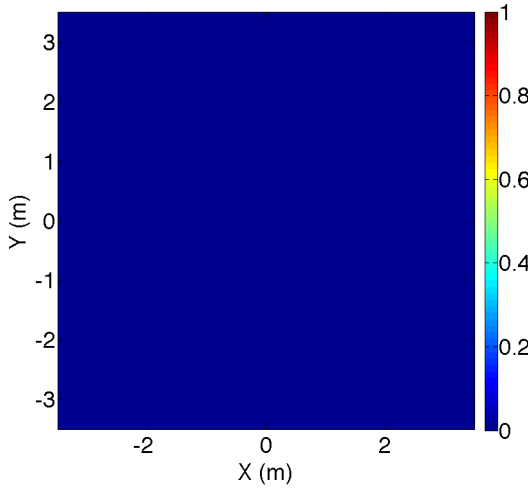


Figure 4.29: Surround configuration polar format image. The node and target locations are indicated by white squares and a white circle, respectively.

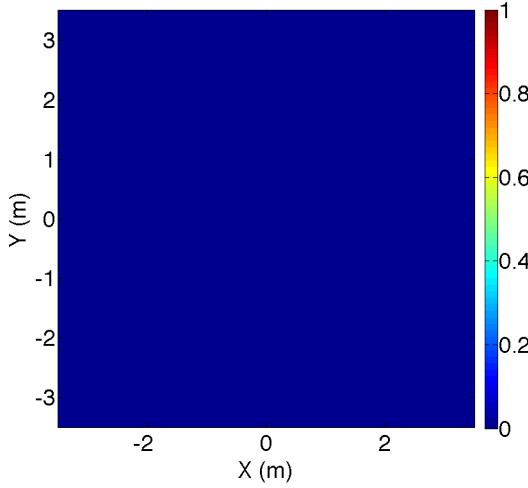


Figure 4.30: Surround configuration polar format image in dB with -3 dB threshold. The node and target locations are indicated by white squares and a white circle, respectively.

As expected from the complexities of the SAR algorithms, their execution times were longer than that of the multilateration algorithm. Table 4.18 shows the ratio of execution time for the polar format algorithm and multilateration. The multilateration algorithm was an average of 34.51, 13.73, and 6.06 times faster than the polar format

Table 4.16: Computational complexity for the Surround configuration using Polar Format Algorithm.

Data Set	Times	Execution Time (s)		
		256 × 256	512 × 512	1024 × 1024
Surround	Interpolation	0.2354	0.4930	1.0937
	Image Formation	0.0057	0.0172	0.0973
	Total	0.2411	0.5102	1.1910

algorithm, depending on image size. Table 4.19 shows that multilateration was an average of 26.67, 20.10, and 16.24 times faster than the backprojection algorithm.

Table 4.20 shows the ratio of execution times for the convolution backprojection and the polar format algorithms. Theoretically, the ratio of execution between the backprojection and polar format algorithms is given by (assuming the polar format algorithm is not dominated by the cost of interpolation)

$$\frac{N^3}{N^2 \log N} = \frac{N}{\log N}. \quad (4.1)$$

This says that for $N = 256$ the polar format algorithm should be approximately 106 times faster than backprojection. The results do not agree with the theoretical; however, this can be explained by modification of the backprojection's complexity. As discussed in Section 2.2.2.2, backprojection has complexity $O(N^3)$ when the image dimensions are $N \times N$ with N projections. In these experiments there were only six or seven projections. Even for the smallest image with $N = 256$, the number of projections is two orders of magnitude smaller. Thus, backprojection algorithms are, in the case of experiments for this thesis, reduced to complexity $O(N^2)$. Additionally, the order of complexity for the polar format algorithm was discussed in Section 2.2.2.1 and given as $P(N) + O(N^2 \log_2 N)$.

Table 4.17: Summary table of all execution times

Data Set	Algorithm	Execution Time (s)		
		256×256	512×512	1024×1024
Arc	Multilateration	0.0066	0.0416	0.2041
	Backprojection	0.1809	0.7712	3.3980
	Polar Format	0.1951	0.4295	1.0507
Line	Multilateration	0.0056	0.0305	0.1792
	Backprojection	0.1514	0.6489	2.8539
	Polar Format	0.2004	0.4355	1.0820
Cluster	Multilateration	0.0066	0.0311	0.1711
	Backprojection	0.1490	0.6363	2.8122
	Polar Format	0.2054	0.4429	1.0945
Surround	Multilateration	0.0058	0.0317	0.1793
	Backprojection	0.1488	0.6385	2.8593
	Polar Format	0.2411	0.5102	1.1910

Table 4.21 shows the ratio of time taken performing the interpolation versus forming the image. You can see that, at most, the image formation process took approximately 16% of the total time.

Table 4.18: Multilateration verses polar format execution times.

Data Set	Execution Time (s)		
	256×256	512×512	1024×1024
Arc	29.56	10.32	5.15
Line	35.79	14.28	6.04
Cluster	31.12	14.24	6.40
Surround	41.57	16.09	6.64
Average	34.51	13.73	6.06

Table 4.19: Multilateration verses convolution backprojection execution times.

Data Set	Execution Time (s)		
	256×256	512×512	1024×1024
Arc	27.41	18.54	16.65
Line	27.04	21.28	15.93
Cluster	22.58	20.46	16.44
Surround	25.66	20.14	15.95
Average	25.67	13.73	16.24

Table 4.20: Polar format verses convolution backprojection execution times.

Data Set	Execution Time (s)		
	256×256	512×512	1024×1024
Arc	0.93	1.80	3.23
Line	0.76	1.49	2.64
Cluster	0.73	1.44	2.57
Surround	0.62	1.25	2.40
Average	0.76	1.49	2.71

Table 4.21: Execution time for the polar format algorithm broken out by interpolation time and image formation time.

Data Set	Component	Execution Time (s)		
		256 × 256	512 × 512	1024 × 1024
Arc	Interpolation	0.1876	0.3999	0.8752
	Image Formation	0.0075	0.0296	0.1755
	Total	0.1951	0.4295	1.0507
	% Interpolation	96.16	93.11	83.30
Line	Interpolation	0.1928	0.4062	0.9064
	Image Formation	0.0076	0.0292	0.1756
	Total	0.2004	0.4355	1.0820
	% Interpolation	96.21	93.29	83.77
Cluster	Interpolation	0.1982	0.4131	0.9201
	Image Formation	0.0073	0.0298	0.1744
	Total	0.2054	0.4429	1.0945
	% Interpolation	96.45	93.27	84.07
Surround	Interpolation	0.2354	0.4930	1.0937
	Image Formation	0.0057	0.0172	0.0973
	Total	0.2411	0.5102	1.1910
	% Interpolation	97.641	96.63	91.83

Table 4.22: Summary table of all measured resolutions

Data Set	Algorithm	ρ_r (m)	ρ_x (m)
Arc	Multilateration	0.5476	1.0743
	Backprojection	0.3914	0.0881
	Polar Format	0.3333	0.9999
Line	Multilateration	0.5496	1.1242
	Backprojection	0.4510	0.0784
	Polar Format	0.3333	0.3333
Cluster	Multilateration	0.5496	2.6232
	Backprojection	0.2157	1.3725
	Polar Format	0.3333	4.3333
Surround	Multilateration	0.6496	1.0743
	Backprojection	0.0588	0.0588
	Polar Format	—	—

V. Conclusions

Covert, high resolution radar imaging is certainly an attractive capability for military applications. Radars that use noise technology have LPI and LPD properties that are the key to this capability. Such technology can be used to provide situational awareness in hostile environments for both military strategists planning from afar and soldiers on the front line. Though the method of data collection must be modified to provide acceptable scene images when using SAR, this research showed that the application of SAR imaging with noise radar data is a viable method of producing high resolution images.

5.1 Review of Research Goals

The goal of this research was to expand on the existing multilateration imaging capability of the AFIT NoNet by utilizing SAR imaging techniques. In addition, this research was used to assess the effect of different configurations of node arrangement on image quality for both multilateration and SAR imaging techniques. The objective was to provide groundwork for future use of the AFIT NoNet as a system capable of covert imaging in a dynamic application, such as a miniaturized set of NoNet nodes mounted on a formation of UAVs.

5.2 Research Results and Contributions

The results presented in Chapter 4 show that SAR imaging techniques are viable for use with a radar system using random noise waveforms. The polar format algorithm, the conventional direct Fourier reconstruction method, was shown to suffer image degradation since its use should be limited to configurations featuring small angle synthetic apertures due to the requirement for interpolation from polar to cartesian grids. Also with a sparse collection of data over the synthetic aperture, the computationally expensive interpolation dominates the overall computational complexity resulting in slow image creation. The

convolution backprojection imaging method was shown to create the best resolution; however, the improved resolution comes with the expense of computational complexity resulting in slow image formation.

Though SAR imaging has shown the ability to create images with improved resolution over multilateration imaging, the configuration, or spatial distribution, and resulting azimuth sampling can have an adverse effect on the image, namely aliasing. For a static system of only six noise radar nodes, azimuth sampling is poor even over a small synthetic aperture and resulting images have a small alias free image extent. Aliasing can result in false targets (copies) and masking or corruption of targets that are outside of the alias free range extent.

Though not ideal, the research verified that it is possible to generate high resolution 2D images using a SAR technique. The issue with SAR imaging with sparse azimuth sampling is that the images can suffer from aliasing making it possible for detection of targets outside of the alias free range to become corrupted and masked by aliased copies. Also, depending on imaging requirements, multilateration imaging, although less fine in resolution, may be able to produce acceptable images depending on node configuration and spatial distribution.

5.3 Future Work

It has been shown that the AFIT NoNet is a viable system for creating 2D images using both multilateration and SAR imaging techniques. However, there are several improvements for possible future work in noise radar imaging using the AFIT NoNet. Some future possibilities include:

1. Augment results with simulations. Simulations of the configurations using ideal targets and scenes that are clutter and RFI free can serve to verify the results of real data and ensure the imaging algorithms are performing as expected. The simulations could provide best case results to compare with measured and calculated results.

2. Incorporation of an amplifier on the transmit chain. During our research, amplifiers arrived but were not incorporated into the system due to timing constraints. The amplifiers are able to increase the transmitted power and thus extend the system's range. It also gives the user the ability to tune the system to take advantage of the full dynamic range of the receive chain A/D converter and improve SNR. If used in close ranges is it important to ensure that the intensity of the receive signal is within the dynamic range of the A/D converter to prevent saturation and degradation of the correlation.
3. Improvements to the SAR convolution backprojection imaging algorithm. In spotlight SAR, the data is collected on a polar grid and since the convolution backprojection algorithm can operate directly on the data collected without the need for interpolation, it is the imaging algorithm that produces images with the finest resolution. In this thesis, the NoNet system of six nodes was used to create a synthetic aperture, thus azimuth sampling, even for relatively short synthetic apertures, was not fine enough to yield acceptable alias free image extents. Since the configurations considered in this thesis were static, the only possible way to form a synthetic aperture was to use each node position. With so few nodes, the execution time for backprojection images seemed insignificant even though by comparison the computational expense was greater than the other imaging algorithms. For an $N \times N$ image with N projections, backprojection has $O(N^3)$ complexity as shown in Section 2.2.2.2. The scenarios of this thesis had only six or seven projections, thus complexity reduced to $O(N^2)$ (this comes from the fact that 256×256 was the smallest image created, in Section 2.2.2.2 $M = 6$ or 7 projections, two orders of magnitude smaller than $N = 256$, and the M term goes away).

In a dynamic system, the group of nodes would move in a formation, making multiple collects from each node possible, thus increasing the azimuth sampling and

increasing the computational expense with the additional radar data collections. The amount of data can grow very quickly and thus increasing complexity. In a dynamic set up as described, the system can quickly reach N projections, bringing complexity back up to $O(N^3)$. When M approaches N projections, the longer execution times will be much more noticeable.

However, fast backprojection algorithms developed for tomography have been adapted to spotlight mode SAR in [23][24]. For $N \times N$ images with N projections [24] claims a fast backprojection complexity of $N^{5/2}$ and [23] claims a complexity of $N^2 \log N$. Application of these algorithms using the AFIT NoNet could reduce the execution time of the SAR backprojection images to times comparable to direct Fourier methods while retaining the advantages associated with backprojection.

4. Application of 3D SAR imaging. With multiple NoNet nodes in a dynamic system, each node collects its own data and can create its own 2D image. By varying the height between the nodes, it is possible to add a third dimension of data and create 3D images.

Bibliography

- [1] Cutrona, LJ. “Synthetic aperture radar”. *Radar Handbook, second edition, ed. M. Skolnik, McGraw-Hill, New York*, 1990.
- [2] Desai, M. D. and W. K. Jenkins. “Convolution backprojection image reconstruction for spotlight mode synthetic aperture radar”. *Image Processing, IEEE Transactions on*, 1(4):505–517, 1992. ID: 1.
- [3] Doerry, Armin W. “Basics of Polar-Format Algorithm for Processing Synthetic Aperture Radar Images”. *Sandia National Laboratories report SAND2012-3369, Unlimited Release*, 2012.
- [4] Gorham, LeRoy A and Linda J Moore. “SAR image formation toolbox for MATLAB”. *SPIE Defense, Security, and Sensing*, 769906–769906. International Society for Optics and Photonics, 2010.
- [5] Hardin, Joshua A. “Information Encoding on a Pseudo Random Noise Radar Waveform”, 2013.
- [6] Jackson, Julie A. “EENG 668/714 Advanced Radar Systems Analysis Class Notes”. Air Force Institute of Technology, 2013.
- [7] Jain, Anil K. *Fundamentals of digital image processing*. Prentice-Hall, Inc., 1989.
- [8] Jakowatz, Charles V, Daniel E Wahl, Paul H Eichel, Dennis C Ghiglia, and Paul A Thompson. *Spotlight-mode synthetic aperture radar: a signal processing approach*, volume 101. Kluwer Academic Publishers Boston, USA:, 1996.
- [9] Kay, Steven. *Intuitive probability and random processes using MATLAB®*. Springer, 2006.
- [10] Levanon, Nadav and Eli Mozeson. *Radar Signals*. John Wiley & Sons, 2004.
- [11] Myers, Aaron T. *The Miniaturization of the AFIT Random Noise Radar*. MS. Thesis, Air Force Institute of Technology, Wright-Patterson AFB, OH, 2013.
- [12] Narayanan, Ram M. “Through-wall radar imaging using UWB noise waveforms”. *Journal of the Franklin Institute*, 345(6):659–678, 2008.
- [13] Narayanan, Ram M. “Ultra-wide-band Noise Radar Systems”. *SPIE Newsroom*, 2012.
- [14] Nelms, Matthew E. *Development and evaluation of a multistatic ultrawideband random noise radar*. MS. Thesis, Air Force Institute of Technology, Wright-Patterson AFB, OH, 2010.

- [15] Passino, Kevin M and Mathew L Moore. *The RCS Handbook: Tools for Real Time Control Systems Software Development*. John Wiley & Sons, Inc., 2001.
- [16] Richards, Mark A, Jim Scheer, and William A Holm. *Principles of modern radar: basic principles*. SciTech Pub., 2010.
- [17] Ross, Raymond Alexander. “Forward scattering from a finite, circular cylinder”. *Progress in Electromagnetics Research C*, 2:207–215, 2008.
- [18] Schmitt, Ashley L. *Radar imaging with a network of digital noise radar systems*. MS. Thesis, Air Force Institute of Technology, Wright-Patterson AFB, OH, 2009.
- [19] Taylor, James D. *Ultra-wideband radar technology*. CRC press, 2000.
- [20] Thayaparan, T and C Wernik. *Noise radar technology basics*. Technical report, DTIC Document, 2006.
- [21] Watson Jr, Raymond C. *Radar Origins Worldwide: History of Its Evolution in 13 Nations Through World War II*. Trafford Publishing, 2009.
- [22] Wilson IV, Russell D. *Adaptations and Analysis of the AFIT Noise Radar Network for Indoor Navigation*. MS. Thesis, Air Force Institute of Technology, Wright-Patterson AFB, OH, 2013.
- [23] Xiao, S., Jr. Munson, D.C., S. Basu, and Y. Bresler. “An N²logN back-projection algorithm for SAR image formation”. *Signals, Systems and Computers, 2000. Conference Record of the Thirty-Fourth Asilomar Conference on*, volume 1, 3–7 vol.1. Oct 2000. ISSN 1058-6393.
- [24] Yegulalp, A.F. “Fast backprojection algorithm for synthetic aperture radar”. *Radar Conference, 1999. The Record of the 1999 IEEE*, 60–65. 1999.

REPORT DOCUMENTATION PAGE

*Form Approved
OMB No. 0704-0188*

The public reporting burden for this collection of information is estimated to average 1 hour per response, including the time for reviewing instructions, searching existing data sources, gathering and maintaining the data needed, and completing and reviewing the collection of information. Send comments regarding this burden estimate or any other aspect of this collection of information, including suggestions for reducing this burden to Department of Defense, Washington Headquarters Services, Directorate for Information Operations and Reports (0704-0188), 1215 Jefferson Davis Highway, Suite 1204, Arlington, VA 22202-4302. Respondents should be aware that notwithstanding any other provision of law, no person shall be subject to any penalty for failing to comply with a collection of information if it does not display a currently valid OMB control number. PLEASE DO NOT RETURN YOUR FORM TO THE ABOVE ADDRESS.

1. REPORT DATE (DD-MM-YYYY)			2. REPORT TYPE		3. DATES COVERED (From — To)	
27-03-2014			Master's Thesis		Oct 2012-Mar 2014	
4. TITLE AND SUBTITLE			5a. CONTRACT NUMBER 5b. GRANT NUMBER 5c. PROGRAM ELEMENT NUMBER 5d. PROJECT NUMBER 5e. TASK NUMBER 5f. WORK UNIT NUMBER			
Comparison of Image Processing Techniques Using Random Noise Radar						
6. AUTHOR(S)			7. PERFORMING ORGANIZATION NAME(S) AND ADDRESS(ES) Air Force Institute of Technology Graduate School of Engineering and Management (AFIT/EN) 2950 Hobson Way WPAFB, OH 45433-7765			
			8. PERFORMING ORGANIZATION REPORT NUMBER AFIT-ENG-14-M-22			
9. SPONSORING / MONITORING AGENCY NAME(S) AND ADDRESS(ES)			10. SPONSOR/MONITOR'S ACRONYM(S) 11. SPONSOR/MONITOR'S REPORT NUMBER(S)			
INTENTIONALLY LEFT BLANK						
12. DISTRIBUTION / AVAILABILITY STATEMENT Distribution Statement A: Approved for Public Release; Distribution Unlimited						
13. SUPPLEMENTARY NOTES This work is declared a work of the U.S. Government and is not subject to copyright protection in the United States.						
14. ABSTRACT <p>Radar imaging is a tool used by our military to provide information to enhance situational awareness for both warfighters on the front lines and military leaders planning and forming strategies from afar. Noise radar technology is especially exciting as it has properties of covertness as well as the ability to see through walls, foliage, and other types of cover. In this thesis, AFIT's NoNet was used to generate images utilizing a random noise radar waveform as the transmission signal. The NoNet was arranged in four configurations: arc, line, cluster, and surround. Images were formed using three algorithms: multilateration and the SAR imaging techniques, convolution backprojection, and polar format algorithm. Each configuration was assessed based on image quality, in terms of its resolution, and computational complexity, in terms of its execution time.</p> <p>Experiments revealed tradeoffs between computational complexity and achieving fine resolutions. Depending on image size, the multilateration algorithm was approximately 6 to 35 faster than polar format and 16 to 26 times faster than convolution backprojection. Backprojection yielded images with resolutions up to approximately 11 times finer in range and 18 times finer in cross-range for the surround configuration, over multilateration images. Pixel size in polar format images made comparisons of resolution unusable.</p> <p>This thesis provides information on the performance of imaging algorithms given a configuration of nodes. The information will provide groundwork for future use of the AFIT NoNet as a covertly operating imaging radar in dynamic applications.</p>						
15. SUBJECT TERMS Noise Radar, Synthetic Aperture Radar, Convolution Backprojection, Multilateration, Polar Format Algorithm						
16. SECURITY CLASSIFICATION OF:			17. LIMITATION OF ABSTRACT	18. NUMBER OF PAGES	19a. NAME OF RESPONSIBLE PERSON Dr. Peter J. Collins, PhD (ENG)	
a. REPORT	b. ABSTRACT	c. THIS PAGE	UU	107	19b. TELEPHONE NUMBER (include area code) (937) 255-3636 ext. 7256 peter.collins@afit.edu	
U	U	U				